

國立臺灣大學理學院大氣科學系



碩士論文

Department of Atmospheric Sciences

College of Science

National Taiwan University

Master Thesis

臺灣東部山區雲霧森林之微氣候韌性

The Resilience of Micro-climate in Eastern Taiwan

Montane Cloud Forest Areas

楊子瑩

Tzu-Ying Yang

指導教授：羅敏輝 博士

Advisor: Min-Hui Lo, Ph.D.

中華民國 112 年 7 月

July, 2023

摘要




頻繁的雲霧籠罩與高相對濕度在雲霧森林的水文氣候循環中扮演重要的角色。在其獨特的微氣候特徵之下，雲霧森林孕育著多樣的物種，使其被視為全球的生物多樣性熱點。然而，過去有許多研究提及雲霧森林在氣候變遷下的脆弱度，其中有眾多文獻強調了氣候變遷下雲霧減少對雲霧森林的影響。相較於整個熱帶而言，臺灣的雲霧森林在森林面積中佔有相對高的比例，但過去有較少文獻針對臺灣的雲霧森林討論其在氣候變遷下所受到的衝擊。本研究透過分析臺灣東部 1980 到 2021 年的降尺度氣候資料，討論雲霧森林與非雲霧森林區域的微氣候在平均態及長期變異上的差異。結果顯示，坐落於中海拔區域的雲霧森林，其白天的相對濕度相較於臺灣東部其他區域有最高的平均量值以及最小的年際變化。當地的高相對濕度可以歸因於其白天大量的水氣來源，以及在克勞修斯-克萊佩龍方程(Clausius-Claypeyron relation)對溫度的非線性影響之下比低海拔地區小得多的飽和水氣量。另一方面，由於雲霧森林及高海拔區域的地表蒸發散量大多取決於當地能量多寡而非可用水量，使當地蒸發散得以調節乾濕年時，地表向大氣的水氣供應。在相近的水氣變化下，雲霧森林相較於高海拔區域更暖的溫度使其白天的相對濕度擁有較小的變化幅度。從相對濕度年際變化的穩定性來看，臺灣東部的雲霧森林展現出相較於其他區域更大的韌性，有別於過去文獻所強調在氣候變遷下雲霧森林的脆弱度。未來研究需更進一步了解外部水氣供應對雲霧森林相對濕度變化的貢獻，並且探討本研究所發現雲霧森林的韌性在未來氣候變遷下是否還將存在。

關鍵字：雲霧森林、相對濕度、微氣候、韌性、氣候變遷

ABSTRACT



Frequent immersion of clouds at ground level and high relative humidity (RH) play vital roles in the hydroclimatological cycle of montane cloud forests (MCFs). These unique microclimates support a wide variety of species, making MCFs renowned as global biodiversity hotspots. However, the vulnerability of MCFs to climate change has been frequently mentioned in previous research, with many studies highlighting the impacts of reduced cloud and fog occurrence on these ecosystems that heavily rely on fog. While some of these studies have examined the conditions of MCFs in Taiwan, there remains a dearth of research on this topic. By analyzing downscaled climate data with a spatial resolution of 2km and a temporal resolution of hourly from 1980 to 2021, our study investigated the microclimate characteristics of MCFs in Eastern Taiwan. We compared these characteristics, including their mean state and long-term variations, with those of non-cloud-forested regions that encompassed all land types other than cloud forests. Our findings revealed that the MCFs, located in the mid-altitudes of Eastern Taiwan, exhibited the highest average daytime RH among the analyzed regions, while displaying the smallest interannual variations. The high mean RH can be attributed to the abundant water vapor supply during the daytime and the nonlinear effect of the Clausius-Clapeyron (C-C) relation on temperature that resulted in much smaller saturated water vapor amounts in the MCFs compared to lower elevations. Both the MCFs and high-



altitude regions experienced energy-limited conditions, regulating their water vapor supply through evapotranspiration in dry and wet years. However, the warmer temperatures in the MCFs contributed to smaller variations in daytime RH compared to high-altitude regions. The high resilience of RH in Eastern Taiwan's MCFs, with minimal interannual variations, suggests a contrast to the vulnerability emphasized in previous studies. Further investigations may be necessary to facilitate our understanding of the contribution of non-local water vapor supply to changes in RH and to determine whether the resilience we found in the MCFs will persist in the face of future climate change.

Keywords: montane cloud forests, relative humidity, microclimate, resilience, climate change

CONTENTS



| | |
|--|----|
| 摘要 | i |
| ABSTRACT | ii |
| CONTENTS | iv |
| LIST OF FIGURES | vi |
| Chapter 1 Introduction | 1 |
| Chapter 2 Data and Methodology | 5 |
| 2.1 Downscaled historical climate data | 5 |
| 2.2 Montane cloud forest map | 8 |
| 2.3 Data analysis..... | 10 |
| 2.3.1 Analyzed regions | 10 |
| 2.3.2 Data processing | 10 |
| Chapter 3 Results | 12 |
| 3.1 Mean state of RH along the altitude | 12 |
| 3.2 Long-term variation of RH along the altitude | 13 |
| 3.2.1 Trends | 13 |
| 3.2.2 Interannual variations | 14 |
| Chapter 4 Discussion..... | 16 |



| | | |
|------------|---|----|
| 4.1 | The roles of water vapor supply and temperature on RH characteristics in MCFs | 16 |
| 4.2 | Relations of annual precipitation and RH in different elevations | 19 |
| 4.3 | Differences in RH characteristics among seasons | 20 |
| 4.4 | RH characteristics in Western Taiwan | 23 |
| 4.5 | Vulnerable or resilient | 24 |
| Chapter 5 | Conclusions | 27 |
| FIGURES | | 30 |
| REFERENCES | | 52 |
| APPENDIX | | 59 |

LIST OF FIGURES



Figure 1. 1 (a) MCF distribution map of Taiwan, with the green area representing MCF areas. (b) Ground fog frequency map of Taiwan. (The figure is from Schulz et al. (2017).)..... 30

Figure 1. 2 (a) Diurnal cycle of relative humidity (% , as a unit) in Chi-Lan MCF (blue) and Lien-Hua-Chih noncloud forest (red). (b) The diurnal frequency of fog occurrence in Chi-Lan (CL) MCF. (The figures are taken from Gu et al. (2021).) 31

Figure 2. 1 Validation of TReAD data. (a) Diurnal cycle of relative humidity [RH (% , as a unit)] in the TReAD grid cell closest to Chi-Lan MCF (blue) and the TReAD grid cell closest to Lien-Hua-Chih noncloud forest (red). (b) Annual rainfall (mm/yr) in Taiwan obtained from TReAD data (blue) and gridded observational data (orange). (c) Annual rainfall (mm/yr) in Eastern Taiwan obtained from TReAD data (blue) and gridded observational data (orange). (d) Fraction of forests derived from the MCF distribution map provided by Schulz et al. (2017). (e) Fraction of forests derived from the land use and land cover map utilized in the TReAD downscaling process..... 32

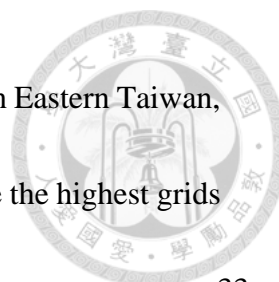
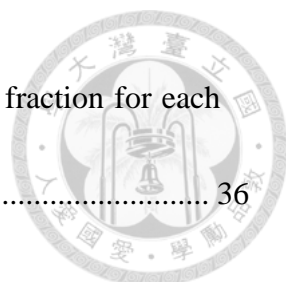


Figure 2. 2 The map of (a) topography in Taiwan, (b) topography in Eastern Taiwan, and (c) cloud forest fraction in Eastern Taiwan. Black dots are the highest grids in each latitude bounded between 23 and 24.5 degree North. 33

Figure 2. 3 Number of grids in each group separated by altitudes of every 50 m starting from an altitude of 0 m. Dots will be marked at the midpoint altitude of each group (e.g., the number of grids of 0 to 50 m will be plotted at an altitude of 25 m). Colors represent the cloud forest fraction averaged for each group, and the scale is the same as in Fig. 2.2c. 34

Figure 3. 1 (a) The relationship between mean daytime relative humidity [RH (% , as a unit)] and altitude (km) in Eastern Taiwan. (b) The relationship between mean daytime specific humidity [Q (g/kg, pattern on the left)] and saturated specific humidity [Qs (g/kg, pattern on the right)] and altitude (km) in Eastern Taiwan. Each dot represents a grid. Colors represent the cloud forest fraction for each grid, and the scale is the same as in Fig. 2.2c. 35

Figure 3. 2 Diurnal cycle of relative humidity [RH (% , as a unit)] along the altitude (km) in Eastern Taiwan. Local time is marked in the upper left of each subplot.



Each dot represents a grid. Colors represent the cloud forest fraction for each grid, and the scale is the same as in Fig. 2.2c. 36

Figure 3. 3 Diurnal cycle of specific humidity [Q (g/kg, patterns on the left of each panel)] and saturated specific humidity [Qs (g/kg, patterns on the right of each panel)] along the altitude (km) in Eastern Taiwan. Local time is marked in the upper right of each panel. Each dot represents a grid. Colors represent the cloud forest fraction for each grid, and the scale is the same as in Fig. 2.2c..... 37

Figure 3. 4 Trends of daytime (a) specific humidity, (b) saturated specific humidity, and (c) relative humidity during 1980-2021 in Eastern Taiwan. Hatched areas have significant trends (p-value < 0.05). Trends are calculated using annual values, but values of relative humidity trend are multiplied by 10 when plotting the colorbar. 38

Figure 3. 5 Anomalies of daytime relative humidity [RH (% , as a unit)] along the altitude (km) for each year in 1980-2021 in Eastern Taiwan. Each dot represents the anomaly of each year compared to 42-year mean in each group. Colors represent the cloud forest fraction averaged for each group, and the scale is the same as in Fig. 2.2c..... 39

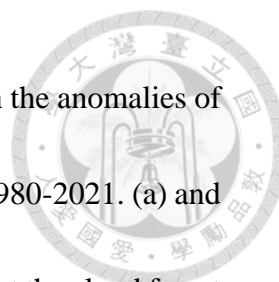


Figure 3. 6 (a, b) Mode 1 and (c, d) mode 2 of the EOF analysis on the anomalies of daytime relative humidity along the altitude for each year in 1980-2021. (a) and (c) are the vertical spatial distributions (EOFs); Colors represent the cloud forest fraction averaged for each group, and the scale is the same as in Fig. 2.2c. (b) and (d) are the time coefficients (PCs). 40

Figure 3. 7 (a) Annual rainfall (mm/yr) in Eastern Taiwan during 1980-2021. (b) The relationship between annual rainfall (mm/yr) in Eastern Taiwan and the time coefficients of mode 1 (PC1) of the EOF analysis on the anomalies of daytime relative humidity along the altitude during 1980-2021..... 41

Figure 3. 8 The relationship between annual rainfall (mm/yr) and annual mean daytime latent heat fluxes (W/m^2) in (a) high altitude, (b) mid altitude, and (c) low altitude (only grids with cloud forest fraction > 0.9 are presented in mid altitude and only grids with cloud forest fraction < 0.1 are presented in high and low altitude). Years and grids are grouped by every 200 mm/yr of rainfall to produce the boxplots. Colors represent the annual mean net radiation (W/m^2) for the average of each group, and the colorbar in (b) fits every panel. Negative values of latent heat fluxes result from the detrending process on grids experiencing land use changes..... 42

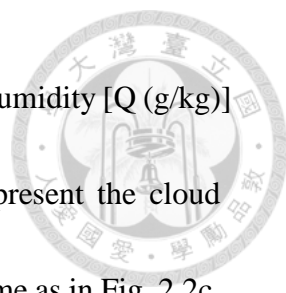
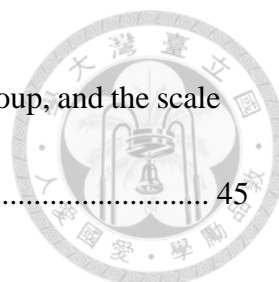


Figure 3. 9 The averaged absolute differences of daytime specific humidity [Q (g/kg)] to the local climatology along the altitude (km). Colors represent the cloud forest fraction averaged for each group, and the scale is the same as in Fig. 2.2c.

..... 43

Figure 4. 1 Schematic plot of mechanisms behind high daytime relative humidity [RH] and small daytime RH variations in Eastern Taiwan’s MCF areas. Thin (thick) arrows refer to mechanisms related to mean state (interannual variation) of RH. + (-) represents increase (decrease) of the pointed term. ET stands for evapotranspiration and T stands for temperature. Color of box regarding non-local transport is lightened as our analysis didn’t focus on its change. 44

Figure 4. 2 The relationship between annual precipitation (mm/yr) and relative humidity [RH (% , as a unit)] in each group. The panels progress from the lowest elevation in the bottom left to the highest elevation in the top right. Values of precipitation and RH are the anomalies compared to local climatology. Black lines are the linear fitting for the relation in each group, and the correlation coefficients for the linear fitting are shown in the lower right of each panel.



Colors represent the cloud forest fraction averaged for each group, and the scale is the same as in Fig. 2.2c. 45

Figure 4. 3 The relationship between mean daytime relative humidity [RH (% , as a unit)] and altitude (km) in Eastern Taiwan in (a) spring (March-May, MAM), (b) summer (June-August, JJA), (c) autumn (September-November, SON), and (d) winter (December-February, DJF). Each dot represents a grid. Colors represent the cloud forest fraction for each grid, and the scale is the same as in Fig. 2.2c. 46

Figure 4. 4 Anomalies of daytime relative humidity [RH (% , as a unit)] along the altitude (km) in (a) spring (March-May, MAM), (b) summer (June-August, JJA), (c) autumn (September-November, SON), and (d) winter (December-February, DJF) for each year in 1980-2021. Each dot represents the anomaly of each year compared to 42-year mean in each group. Colors represent the cloud forest fraction averaged for each group, and the scale is the same as in Fig. 2.2c. 47

Figure 4. 5 The map of (a) topography and (b) cloud forest fraction in Western Taiwan. Black dots are the highest grids in each latitude bounded between 23 and 24.5 degree North. 48

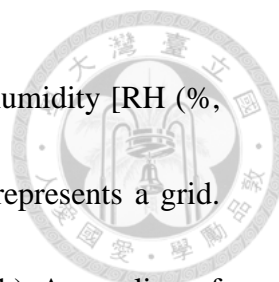
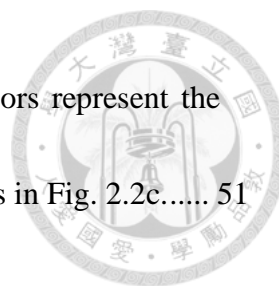


Figure 4. 6 (a) The relationship between mean daytime relative humidity [RH (%,
as a unit)] and altitude (km) in Western Taiwan. Each dot represents a grid.
Colors represent the cloud forest fraction for each grid. (b) Anomalies of
daytime relative humidity [RH (% , as a unit)] along the altitude (km) for each
year in 1980-2021 in Western Taiwan. Each dot represents the anomaly of each
year compared to 42-year mean in each group. Colors represent the cloud forest
fraction averaged for each group. The scale of colors in (a) and (b) are the same
as in Fig. 2.2c..... 49

Figure 4. 7 Differences of mean daytime values of 5 meteorological variables
between the 4K-enhanced scenario (4K) and baseline in Eastern Taiwan: (a)
specific humidity [Q (g/kg, pattern on the left)] and saturated specific humidity
[Qs (g/kg, pattern on the right)], (b) latent heat fluxes [LH (W/m²)], (c) relative
humidity [RH (% , as a unit)], and (d) temperature [T (°C)]. Each dot represents
a grid. Colors represent the cloud forest fraction for each grid, and the scale is
the same as in Fig. 2.2c..... 50

Figure 4. 8 Proportional increase of (a) specific humidity and (b) saturated specific
humidity from baseline to the 4K-enhanced scenario (4K) relative to their mean



state values in the baseline. Each dot represents a grid. Colors represent the cloud forest fraction for each grid, and the scale is the same as in Fig. 2.2c..... 51

Figure A 1 The time series of annual precipitation (mm/yr) in each group. The panels progress from the lowest elevation in the bottom left to the highest elevation in the top right. Values are the anomalies compared to local climatology. Black lines are the linear fitting for the trend in 1990-2021 in each group. Colors represent the cloud forest fraction averaged for each group, and the scale is the same as in Fig. 2.2c..... 59

Figure A 2 The time series of relative humidity [RH (% , as a unit)] in each group. The panels progress from the lowest elevation in the bottom left to the highest elevation in the top right. Values are the anomalies compared to local climatology. Black lines are the linear fitting for the trend in 1990-2021 in each group. Colors represent the cloud forest fraction averaged for each group, and the scale is the same as in Fig. 2.2c. 60

Chapter 1 Introduction

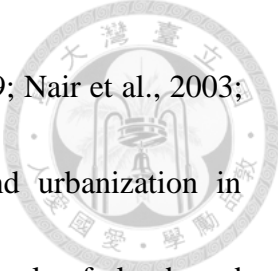


Montane cloud forests (MCFs) are characterized by frequent, persistent, or seasonal ground-level cloud immersion (Grubb, 1977; Hamilton et al., 1993). They are recognized as global biodiversity hotspots, harboring a wide variety of endemic species (Bubb et al., 2004; Bruijnzeel, Scatena et al., 2011). The distribution of MCFs is dictated by the juxtaposition of forest vegetation type and ideal fog formation conditions, thus defining characteristics include latitude, altitude, wind field, rainfall pattern, size of mountains, and the distance from the ocean (Bubb et al., 2004). The MCF ecosystem is unique as the hydroclimatological cycle is intimately connected to the persistent presence of clouds and fog (Still et al., 1999). Clouds and fog in these forests obscure incoming shortwave radiation, resulting in lower available energy. Conversely, at the vegetation level, MCFs benefit from the interception of cloud water by vegetation and the soil surface, thereby enhancing the available water (Stadtmüller, 1987; Hamilton et al., 1993; Bruijnzeel, Mulligan et al., 2011). The moist environment in MCFs is particularly favorable for the growth of epiphytes (Lai et al., 2021), which act as water reservoirs, regulating flood events and maintaining water storage throughout the year (Still et al., 1999; Chang et al., 2002; Mildenerger et al., 2009; Fischer et al., 2016; Schulz et al., 2016). Evapotranspiration from the forest canopy also contributes to the release of abundant

water vapor into the atmosphere (Forzieri et al., 2020), further promoting the humid conditions in MCFs.




Despite being a unique ecosystem, past studies have emphasized the vulnerability of MCFs to anthropogenic development and climate change among tropical forest ecosystems. A review of the literature on the impacts of climate change on MCFs showed that these forests are more susceptible to the effects of climate change (Mata-Guel et al., 2023). A more rapid warming is predicted and observed at high elevations than at lower elevations (Beniston et al., 1997; Foster, 2001; Pepin et al., 2022). This temperature rise, along with alterations in rainfall patterns, leads to an upward shifting in the climatic optimum for montane ecotones. Consequently, MCFs may be replaced by ecosystems at lower altitudes, which may have weaker constraints on invasive species and could potentially lead to the extinction of MCFs originally situated on mountaintops (Foster, 2001; Pauchard et al., 2009; Oliveira et al., 2014). In addition to changes in temperature and precipitation, alterations in cloudiness are a commonly stated concern for MCFs. An increase in air temperature, leading to greater dew point depression, and thus a shift of the condensation level to higher altitudes (Williams et al., 2015), has been predicted in modeling results (Still et al., 1999). This suggests a potential decrease in cloud and fog occurrence in altitudes that were previously immersed in fog. Indeed, shifts in cloud-forming level, or cloud lifting, in MCFs has been shown in past records by a reduction of




cloud-fog incidence and mist and fog occurrence (Pounds et al., 1999; Nair et al., 2003; Williams et al., 2015), with cases attributed to deforestation and urbanization in neighboring areas as well as climate changes. In view of the crucial role of clouds and fog in MCF ecosystems, drier atmospheric conditions associated with a reduction of fog may have adverse effects on their microclimate and hydrological cycle, potentially leading to a decline in endemism and particularly moisture-sensitive species in MCFs (Pounds et al., 1999; Foster, 2001; Oliveira et al., 2014).

In the tropics, MCFs are estimated to occupy 1.4% of the global tropical forests (Bruijnzeel, Mulligan et al., 2011), whereas specifically in Taiwan, MCFs account for approximately 27% of the country's forested area and are predominantly located at altitudes ranging from about 1500 to 2500 m above sea level (Schulz et al., 2017, Fig. 1.1a). Previous studies have examined the relationship between diurnal fog occurrence, near-surface relative humidity (RH), and the hydroclimatological cycle in the Chi-Lan MCF of Northeastern Taiwan (Chu et al., 2014; Gu et al., 2021; 1650 m a.s.l.). These studies have found that the highest RH in the Chi-Lan MCF occurs in the afternoon (Fig. 1.2a), coinciding with the peak frequency of fog (Fig. 1.2b). The distinctive daytime increase in RH in the Chi-Lan MCF, contrasting with the daytime decreasing RH in the Lien-Hua-Chih noncloud forest (780 m a.s.l.) in Central Taiwan, can be attributed to a steep increase in water vapor and a lower daytime temperature. Yet, it remains unclear



whether the mechanisms observed in this specific site can be generalized to a broader MCF area. Additionally, there is a lack of studies investigating the specific impacts of climate change on MCFs in Taiwan, despite their significant presence within forested areas. In particular, a deeper understanding of the mechanisms behind the microclimate characteristics in MCFs in Taiwan and how they may change in the future is crucial. Moreover, although numerous studies have investigated the impacts of climate change on MCFs from various aspects, there is limited research that has utilized long-term (≥ 10 years) data to examine these impacts (Mata-Guel et al., 2023). Thus, the availability of over 40 years of downscaled historical climate data, including near-surface atmospheric conditions for the entire Taiwan region, through the Taiwan Climate Change Prediction Information and Adaptation Knowledge Platform (TCCIP) presents a great opportunity to bridge these research gaps. By analyzing this data, our study aims to explore the differences in microclimate characteristics between MCFs and non-cloud-forested regions (including all land types other than cloud forests, such as other forest types, farm land, urban areas, etc.), as well as investigate the changes that have occurred within the MCFs compared to non-cloud-forested areas over the past few decades. Considering the differences in mean RH along altitudes between Eastern and Western Taiwan (as depicted in Fig. 3.1a for the East and Fig. 4.6a for the West; the detailed method on the separation of Eastern and Western Taiwan will be described in Section 2.3.1, and the specific

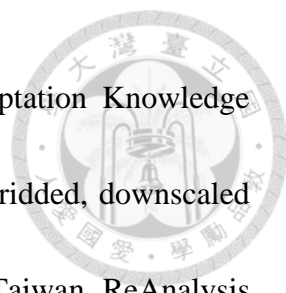


patterns of RH will be discussed in Sections 3.1 and 4.4), as well as the higher occurrence of ground fog in Eastern Taiwan compared to the west (Schulz et al., 2017, Fig. 1.1b), our study focuses on Eastern Taiwan. Through an examination of both mean state and long-term variations, we seek to identify the distinct features of the microclimate in the MCFs and elucidate the underlying mechanisms driving these differences.

Chapter 2 Data and Methodology

To better examine regional near-surface atmospheric characteristics over Taiwan, there is a need for higher spatial resolution data (i.e., 2 km) compared to that of reanalysis data. To address this requirement, regional climate models were utilized for dynamic downscaling processes. This approach not only overcomes the limitation of spatial resolution (i.e., 25 km) in reanalysis data but also helps mitigate the challenges posed by the scarcity and uneven density of observational data. For our study, we focused on analyzing land surface parameters in Eastern Taiwan using downscaled historical climate data spanning from 1980 to 2021. To differentiate between MCFs and non-cloud-forested regions, we utilized the MCF map of Taiwan developed by Schulz et al. (2017) as a reference. By matching the atmospheric characteristics in the downscaled climate data to the fraction of MCFs in each grid, we were able to assess the differences between these two types of regions.

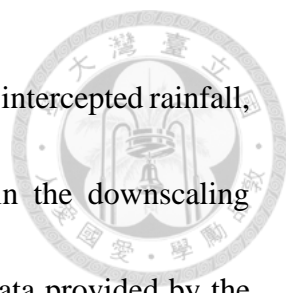
2.1 Downscaled historical climate data



The Taiwan Climate Change Projection Information and Adaptation Knowledge Platform (TCCIP, <https://tccip.ncdr.nat.gov.tw>) provides regional, gridded, downscaled climate data for Taiwan. For our analysis, we employed the Taiwan ReAnalysis Downscaling data (TReAD) from TCCIP, as introduced by Lin et al. (2021). TReAD consists of high-resolution historical data covering the entire Taiwan region. It was obtained through dynamic downscaling techniques using the Weather Research and Forecasting (WRF) model, version 3.8.1 (Skamarock et al., 2008), with the fifth generation ECMWF atmospheric reanalysis (ERA5) data (European Centre for Medium-Range Weather Forecasts [ECMWF], 2017) as the basis.

To ensure the accuracy of the downscaling process and prevent the amplification of errors over time, the WRF downscaling process applied a re-initialization method, as described by Kayaba et al. (2016). This involved starting a new short-term simulation every 6 hours. The initial and boundary conditions for the downscaling process were derived from the ERA5 data. The short-term simulated output of the WRF model was then combined with the ERA5 data using a blending technique (Yang, 2005a, b), which served as the initial condition for the subsequent short-term simulation.

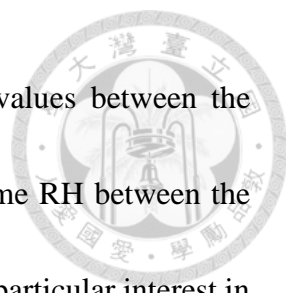
Noah Land Surface Model (Chen, 2007) was utilized for the parameterization of land surface processes in the downscaling process, where latent heat flux from the land surface was obtained through the sum of its components, including direct evaporation from the



soil, transpiration through the plant canopy, evaporation from canopy-intercepted rainfall, and sublimation from the snowpack. The topography data used in the downscaling process was based on the global multi-resolution terrain elevation data provided by the U.S. Geological Survey and the National Geospatial-Intelligence Agency (Danielson & Gesch, 2011). Regarding land use and land cover, the downscaling process incorporated data provided by Chen et al. (2019). The data includes information on land use and land cover changes in Taiwan during four stages: 1980-1988, 1989-1997, 1998-2007, and 2008-2021. It's important to note that while the land use and land cover information changes from stage to stage, it remains unchanged within each individual stage.

We analyzed 42 years of land-surface data from 1980 to 2021 in TReAD, including temperature, specific humidity, saturated specific humidity, relative humidity, precipitation, and latent heat flux. The temporal resolution of the data is one hour, and the spatial resolution is 2 km. Temperature and specific humidity data are values at a height of 2 meters above the surface. These two variables together with surface pressure were used to calculate saturated specific humidity and relative humidity.

Relative humidity data in TReAD was validated by comparing with the diurnal patterns observed in the Chi-Lan MCF and Lien-Hua-Chih noncloud forest, as reported by Gu et al. (2021). We selected the grid in the TReAD dataset that was closest to the location of Chi-Lan MCF and another grid closest to the Lien-Hua-Chih site for the RH



comparison. Although there were slight differences in the mean values between the TReAD data and the observed values, the diverse patterns of daytime RH between the Chi-Lan MCF and the Lien-Hua-Chih noncloud forest, which are of particular interest in our study, were captured in the TReAD data (Fig. 2.1a). Additionally, we compared the annual mean precipitation in Taiwan, as well as specifically in Eastern Taiwan, obtained from TReAD with gridded observational data (Fig. 2.1b, Fig. 2.1c). The comparison revealed a comparable interannual variation in precipitation between the two datasets, although the TReAD data generally exhibited slightly higher precipitation values.

2.2 Montane cloud forest map

Schulz et al. (2017) developed a map of MCF distribution in Taiwan (Fig. 1.1a) by combining an MCF condition map and a forest map. The MCF condition map was created using the Random Forest machine learning method. Various input data were used in the machine learning process, including: (1) ground fog frequency generated using the MODIS daytime scene, which covered Taiwan from 2003 to 2014, with the fog detecting algorithm called Detection of Ground Fog in Mountainous Areas (DOGMA) applied to determine the frequency of fog occurrence; (2) altitude and other topographic information extracted or calculated from ASTER GDEM 2, a digital elevation model dataset; (3) Landsat 7 Enhanced Thematic Mapper Plus (ETM+) visible and shortwave infrared bands from 1999 to 2003; (4) geostatistical texture images of the Landsat composites. Training



data points for the MCF conditions were taken from the National Vegetation Database of Taiwan and classified to “MCF” and “non-MCF”.

Areas classified by the machine learning method as having MCF conditions may include both forested and non-forested regions. Therefore, a Random Forest model was trained based on locations classified as forest and non-forest, aiming to create a forest map for Taiwan that could be combined with the map of MCF conditions.

The MCF distribution map has a spatial resolution of 250 m, with each pixel classified into categories including montane cloud forest, other forest, no forest, or MCF conditions in non-forest areas. To match the 2-km resolution of TReAD, we aggregated adjacent 8x8 grid cells in the MCF map and calculated the cloud forest fraction for each grid in TReAD using the following Eq. (1):

$$\text{cloud forest fraction} = \frac{MCF}{MCF + OF + NF + NF_{MCF}} \quad \dots (1)$$

where MCF is montane cloud forest, OF is other forest, NF is no forest, and NF_{MCF} is MCF conditions in non-forest areas, each term showing the number of grids of a specific category within the 8x8 grid cells. The calculated fraction of forests, including both montane cloud forests and other forests (Fig. 2.1d), roughly matched with the forest fraction derived from the land use and land cover map utilized in the TReAD downscaling process (Fig. 2.1e), while the latter had more values close to 0 or 1 due to the coarser

spatial resolution of TReAD data (2 km) compared to that of the MCF distribution map (250 m).



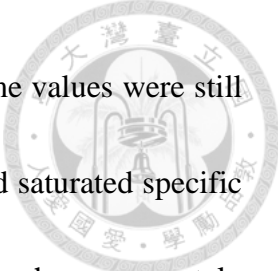
2.3 Data analysis

2.3.1 Analyzed regions

Grids representing Eastern Taiwan were selected based on the topography of Taiwan (Fig. 2.2a). The northernmost and southernmost regions of Taiwan were excluded to concentrate on latitudes that encompass the highest proportion of MCFs and all altitude ranges. The remaining latitudes ranged from around 23 to 24.5 degree North. Within each latitude band, the grid with the highest altitude was identified (shown as black dots in Fig. 2.2a), and grids situated to the east of these highest grids were selected as the regions of interest for our analysis (Fig. 2.2b, c).

2.3.2 Data processing

Mean values and annual anomalies of relative humidity (RH) and related variables were calculated to analyze the mean state and long-term variations over the 42-year period. The 42-year mean values were computed without detrending, while the annual anomalies of RH were determined after detrending temperature and specific humidity (Q) in each grid using their annual mean whole-day values. Our focus on the 42-year mean values and annual anomalies primarily pertained to daytime values, when shortwave radiation values were greater than zero, aiming to capture potentially significant differences in RH



patterns between the MCFs and non-cloud-forested regions. Nighttime values were still utilized when zooming in to examine the diurnal cycle of RH, Q, and saturated specific humidity (Qs). The diurnal analysis included patterns from night to day, shown separately, to gain insights into the formation of the daytime characteristics.

To simplify the analysis of interannual variabilities, the grid cells were grouped based on altitude, with each group spanning a 50-meter interval (Fig. 2.3). The lowest-altitude groups contained the largest number of grids (i.e., between 40-60 grids for the lowest five groups), while the highest-altitude groups had the fewest (i.e., less than 10 grids for the highest five groups). Anomalies of annual mean daytime RH along the altitude were calculated for each year by subtracting the 42-year mean value from the annual mean daytime RH of each year of each altitude group.

To examine the interannual variations of daytime RH in all altitude groups, we further applied Empirical Orthogonal Function (EOF) analysis using the Python package "*eofs*" (Dawson, 2016). By employing the EOF technique, we transformed the spatial-temporal data (altitude groups-annual) into vertical profiles that capture the patterns of variance (referred to as empirical orthogonal functions, EOFs), accompanied by corresponding time series that illustrate the contribution of each profile to the year-to-year variation (known as principal components, PCs). In the EOF analysis, we did not consider the

number of grids as weights for each altitude group, as our focus was on capturing changes in the patterns of the mean value of each group for each year.

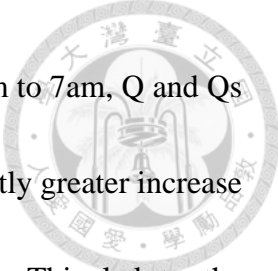


Chapter 3 Results

3.1 Mean state of RH along the altitude

A nonlinear relationship was observed between mean daytime relative humidity (RH) and altitude in Eastern Taiwan from 1980 to 2021 (Fig. 3.1a). The highest daytime RH values were found in the mid-altitude range of approximately 1000 to 2500 m, where MCFs were most abundant. This nonlinear pattern of RH along altitude was attributed to the patterns of both daytime specific humidity (Q) and saturated specific humidity (Q_s) (Fig. 3.1b). Q_s exhibited an upward concave pattern, while Q showed a downward concave pattern. In the low altitudes, where near-surface temperatures are high, the nonlinear effect of the Clausius-Clapeyron (C-C) relation further contributed to a greater change in Q_s along the altitude. On the other hand, this nonlinear effect resulted in smaller differences in Q_s between the high and mid-altitudes. Additionally, Q decreased with increasing altitude, but the rate of decrease was higher in higher regions compared to the pattern of Q_s .

Throughout the diurnal cycle, RH displayed distinct patterns (Fig. 3.2), accompanied by varying characteristics of Q and Q_s over time (Fig. 3.3). During the nighttime period from 9pm to 5am, RH showed less variations across different altitudes, and both Q and



Qs exhibited upward concave patterns. As the sun rose at around 6 am to 7am, Q and Qs increased at all altitudes. Among these regions, there was a significantly greater increase in Q in the MCFs compared to the higher and lower altitudes. This led to the disappearance of the upward concave pattern in Q and an increase in RH in the MCFs, while other regions experienced a decrease in RH. The abundant water vapor supply during this time included local evapotranspiration as well as non-local water vapor brought by valley winds. In the late morning, Q continued to show the greatest increase in the MCF regions and exhibited a clear downward concave pattern around noontime. In the afternoon, starting from around 1pm, Qs started to decrease. Q and Qs in the MCF regions reached their closest proximity at around 3pm to 5pm, corresponding to the time of the highest RH in the MCFs during the day.

3.2 Long-term variation of RH along the altitude

3.2.1 Trends

Daytime Qs over the past 42 years exhibited significant increasing trends (p-value < 0.05) in most studied areas, with greater trends found in coastal low-altitude regions (Fig. 3.4b). Concurrently, daytime Q also showed significant increases (p-value < 0.05) in most areas during these warming trends (Fig. 3.4a). However, except for regions that have undergone land-use changes in the past 42 years, daytime RH did not display significant trends in Eastern Taiwan (Fig. 3.4c).



3.2.2 Interannual variations

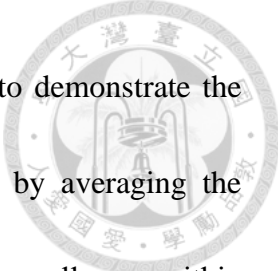
The spread of anomalies of annual mean daytime RH along the altitude for 42 years displayed a corset-shaped pattern (Fig. 3.5), indicating greater interannual variations in high and low altitudes and smaller variations in the mid altitudes. An EOF analysis was conducted on this pattern of Fig. 3.5 to identify the dominant patterns of interannual variations in daytime RH along the altitude. The first two modes accounted for 76.4% and 17.0% of the total variance, respectively. Fig. 3.6 illustrates the vertical spatial distributions (EOFs) and the principal component (PCs) time series of the first two modes. In mode 1, daytime RH exhibited the same sign across all altitudes, with the least fluctuation from the mean value in the mid altitudes (Fig. 3.6a). Mode 2 demonstrated a nearly monotonic change along the altitude, with opposite signs in high and low altitudes, while the changes in the mid altitudes remained relatively weak (Fig. 3.6c). These two modes corresponded to the smaller variations in the mid altitudes as interpreted from the corset-shaped pattern (Fig. 3.5). In addition, the time coefficients in mode 1 (Fig. 3.6b) exhibited a negative correlation with the mean annual rainfall in the studied region (Fig. 3.7a, b). This indicated that when the annual rainfall in Eastern Taiwan was less, daytime RH tended to be lower than the climatology values at all elevations, with a potentially weaker decrease in the mid altitudes. Similarly, during periods of above-average annual

rainfall, the increase in RH might be weaker in the mid altitudes compared to other regions.



We propose that the different responses of RH to precipitation in the mid altitudes compared to other regions are related to the availability of water and energy in these areas. In regions with sufficient precipitation, local latent heat fluxes may be primarily limited by energy. As a result, even in dry years, there is still enough water for evapotranspiration, which supplies water vapor to the atmosphere and helps stabilize the changes in RH. Moreover, evapotranspiration in these regions may even increase during dry years due to higher net radiation under less cloudy conditions. On the other hand, in water-limited regions, there is less water available for evapotranspiration during dry years, leading to a more sensitive response of RH to dry conditions.

Fig. 3.8 illustrates the relationship between annual rainfall and daytime latent heat fluxes at different altitudes. In the low altitudes, net radiation was typically high, while precipitation was generally lower compared to the high and mid altitudes (Fig. 3.8c). Evapotranspiration decreased when annual precipitation dropped below approximately 2000 mm, showing a water-limited condition in these areas. In contrast, both net radiation and evapotranspiration increased during dry years in the high and mid altitudes (Fig. 3.8a, b), indicating energy-limited conditions in both regions that regulated the supply of water vapor in wet and dry years.

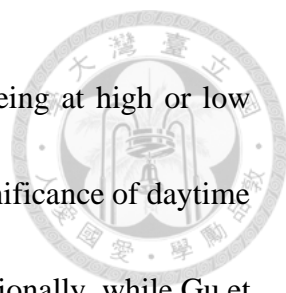


The deviation of daytime Q from the climatology was derived to demonstrate the fluctuations of daytime Q at different altitudes. It was calculated by averaging the absolute differences between each year's value and the mean value across all years within each altitude group. Fig 3.9 illustrates a similar fluctuation of daytime Q in the high and mid altitudes above approximately 2000 m. However, since the mean state temperature and mean state Q_s are lower in the high altitudes compared to the mid altitudes, similar fluctuations in Q may have a greater influence on the variations of RH in high-altitude regions. Consequently, although both high and mid altitudes experienced energy-limited conditions, the lower temperatures in high elevations contributed to greater interannual variations in RH.

Chapter 4 Discussion

4.1 The roles of water vapor supply and temperature on RH characteristics in MCFs

Our study in Eastern Taiwan reveals the unique characteristics of high daytime RH and the distinct increase in RH after sunrise in the MCF areas compared to higher and lower altitudes. Building upon the work of Gu et al. (2021), which focused on a single MCF site and a noncloud forest site at a lower altitude, our study expands the analysis to a larger area in Eastern Taiwan. The diurnal patterns of RH we found align with Gu et al. (2021), indicating that the MCFs and non-cloud-forested regions exhibit opposite changes



in RH after sunrise, regardless of the non-cloud-forested regions being at high or low altitudes. Our study supports Gu et al. (2021) in emphasizing the significance of daytime near-surface water vapor as a source for high RH in the MCFs. Additionally, while Gu et al. (2021) highlighted the importance of slowly increasing daytime temperature in the MCF site, we further emphasize the nonlinear effect of the C-C relation, which leads to even greater differences in Q_s between mid and low altitudes (Fig. 4.1, indicated by thin arrows).

The distinctive features of the near-surface water vapor source and temperature are also crucial factors contributing to the low interannual variability of daytime RH in Eastern Taiwan's MCFs. Under energy-limited conditions, the water vapor source from local evapotranspiration in mid and high altitudes is enhanced during dry years and reduced during wet years. Additionally, although fluctuations in water vapor are regulated in both high and mid altitudes, the warmer temperatures and higher Q_s in mid altitudes result in smaller variations in RH for the MCFs in Eastern Taiwan (Fig. 4.1, indicated by thick arrows).

We also conducted analyses of the pattern of mean daytime vapor pressure deficit (VPD) and the interannual variations of daytime VPD along the altitude (figures not shown). However, due to the effect of the monotonic change in temperature on water vapor pressure, we observed a general decrease in both mean state and interannual

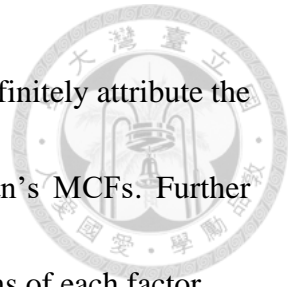
variations of VPD with increasing elevation. This was in contrast to the patterns seen in the analysis of RH, which was normalized by the values of Q_s .



Indeed, the examination of non-local water vapor supply is an important aspect that was not addressed in our study. Changes in non-local water vapor supply, particularly related to the water vapor amount in neighboring areas and the strength of mountain-valley winds, can significantly influence the interannual variations of RH in MCFs and its potential changes under future warming. To gain a more comprehensive understanding of the mechanisms driving the microclimate in MCFs, further simulations of water vapor trajectories are necessary to quantify both the local and non-local supply.


The unique RH features in Eastern Taiwan's MCFs can be attributed to several factors. The presence of fog, for instance, plays a positive role in the microclimate of MCFs. It provides water through interception as additional available water for evapotranspiration and obscures incoming solar radiation that potentially reduces temperatures. This creates a more favorable environment for fog occurrence and forms a positive feedback loop by enhancing RH values and contributing to the stability of interannual RH patterns in MCFs. Additionally, the dense vegetation within the MCFs acts as a significant local source of water vapor, contributing to the observed RH patterns. Furthermore, the favorable altitude and location of the MCFs provide suitable conditions such as appropriate temperatures and mountain-valley winds, which support the unique RH characteristics. However, due

to the interconnection of various factors, it remains challenging to definitely attribute the primary cause of the distinct RH characteristics in Eastern Taiwan's MCFs. Further model experiments are needed to examine the individual contributions of each factor.




4.2 Relations of annual precipitation and RH in different elevations

The relationship between PC1 of EOF analysis and mean annual precipitation in Eastern Taiwan (Fig. 3.7b) demonstrated that the response of daytime RH to annual precipitation in the analyzed region was weaker in the MCFs compared to higher and lower altitudes. It should be noted that precipitation can vary among altitudes and grids, leading to various effects on changes in RH. Fig. 4.2 shows the relationships between annual precipitation and daytime RH in different groups separated by altitudes. We observed the smallest range of RH in the mid altitudes, which corresponded to the corset shape depicted in Fig. 3.5. On top of that, while there was a positive relationship between annual precipitation and daytime RH in all altitudes, the strength of this relationship differed between groups. In the low altitudes, precipitation and daytime RH exhibited the strongest correlation, whereas the correlation was weakest in the mid altitudes. This confirmed that RH in Eastern Taiwan's MCFs had the weakest response to annual rainfall, regardless of whether it was based on the mean precipitation of Eastern Taiwan or the local value.



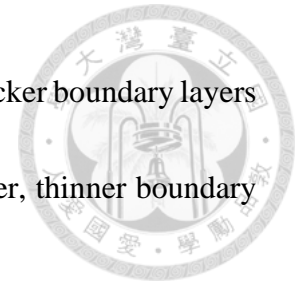
Mode 2 of the EOF analysis revealed the smallest change and potential resilience of RH in the mid altitudes, similar to mode 1. However, unlike mode 1, mode 2 showed opposite behavior of RH in high- and low- altitude regions (Fig. 3.6c). Additionally, the time coefficients in mode 2 exhibited a decreasing trend in the last 32 years (Fig. 3.6d, 1990-2021), which may be related to the decreasing pattern of Eastern Taiwan's mean annual rainfall during the same period (Fig. 3.7a). To further explore the relationship between the trends of annual rainfall and daytime RH from 1990 to 2021, we analyzed the time series of annual mean daytime RH and precipitation in different altitudes (Figs. A1 and A2). Fig. A1 illustrates a consistent decrease in precipitation across all elevations from 1990 to 2021, while the patterns of daytime RH during this period varied among the altitudes (Fig. A2). In the low altitudes, RH decreased in accordance with the declining annual rainfall. Conversely, RH increased in the high and mid altitudes despite the reduced precipitation, with a milder rise in the mid altitudes. The opposite relationships between the trends of precipitation and daytime RH in 1990-2021 in high and low altitudes aligned with the opposite pattern of RH in mode 2 of the EOF analysis. However, the trends of daytime RH in 1990-2021 were not significant across the altitudes; instead, the variations of RH during this period were primarily influenced by their interannual fluctuations.

4.3 Differences in RH characteristics among seasons



Synoptic weather patterns in Taiwan exhibit notable variations across seasons, with distinct dominant monsoons and other atmospheric processes contributing to diverse climate characteristics. Notably, the ground fog frequency map of Taiwan by Schulz et al. (2017), reveals that the eastern slope of the Central Mountain Range experienced higher fog occurrence during winter months compared to summer, primarily associated with the presence of the winter monsoon. Considering the observed disparities in fog frequency throughout the seasons, differences in RH patterns along the altitude may also be pronounced. Fig. 4.3 illustrates the changes in mean daytime RH along the altitude in four seasons: spring (March-May, MAM), summer (June-August, JJA), autumn (September-November, SON), and winter (December-February, DJF). Nonlinear patterns can be seen throughout all separated seasons. The greatest differences between seasons occurred in the variations of daytime RH from mid-elevation to high-elevation areas. In spring, autumn, and the annual average (Fig. 4.3a, c, and Fig. 3.1a), daytime RH started to decrease from the mid altitudes to the high altitudes, resulting in the highest daytime RH values in the mid altitudes. During winter, RH also decreased from mid to high elevations, with a stronger decrease contributing to greater differences between the MCFs and non-cloud-forested regions (Fig. 4.3d). In contrast, during summer, the differences in daytime RH between mid and high altitudes were less pronounced (Fig. 4.3b). We speculate that such differences in high altitudes between winter and summer may be

attributed to the characteristics of seasonal monsoons. In summer, thicker boundary layers allowed for more water vapor to reach high altitudes, while in winter, thinner boundary layers restricted high RH to mid-elevations.



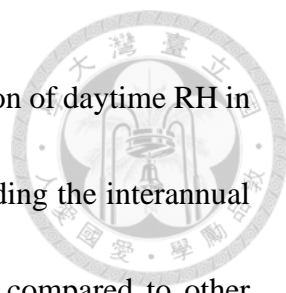
To assess the interannual variability of daytime RH in different seasons, we calculated RH for each season by detrending the temperature and specific humidity in each grid using the trends of the annual mean values for each season. Fig. 4.4 shows the spread of anomalies of annual mean daytime RH along the altitude for 42 years in the four seasons. While the overall corset-shaped pattern with minimal variations in the MCFs was observed in the annual result (Fig. 3.5), this pattern was influenced by varying characteristics of vertical patterns in different seasons. The same corset shape with minimal variations in the MCFs was only evident in autumn (Fig. 4.4c). During winter and spring, the smallest variations in daytime RH occurred at the intersection of the MCFs and low altitude non-cloud-forested areas (Fig. 4.4a, d). Furthermore, a more pronounced variation was found in the high altitudes compared to the low altitudes, particularly during winter. We speculate that this great variation in the high altitudes may be associated with the lower temperatures experienced in these regions during winter and spring, similar to the mechanisms proposed for the differences in RH variations between mid and high altitudes in the annual analysis. Conversely, the reduced variation in high altitudes during

summer (Fig. 4.4b) may be attributed to the relatively warmer temperature compared to other seasons.



4.4 RH characteristics in Western Taiwan

Eastern and western Taiwan exhibit differences in various aspects, including topography and the influence of the monsoon. Schulz et al. (2017) established a connection between the lower occurrence of fog on the western slopes of the Central Mountain Range, especially during winter, and the presence of the winter monsoon. They also mentioned the Massenerhebung effect, which contributed to more frequent ground fog in lower altitudes within isolated mountain terrains like the Hai-an Range in eastern Taiwan. Considering these observed disparities in fog frequency, it is likely that RH patterns also display distinct features between eastern and western Taiwan. We conducted an analysis of daytime RH patterns in the western part of Taiwan, within the 23 to 24.5-degree North latitude range (Fig. 4.5). The western region exhibited a relatively smaller cloud forest fraction, with areas of higher cloud forest fraction occurring at higher altitudes, around 1500 to 2500 m above sea level, compared to the 1000 to 2500-meter range in eastern Taiwan. When examining the mean daytime RH along the altitude, we discovered a less pronounced nonlinear pattern in the west compared to the east, with similar RH values at high altitudes as in mid altitudes (Fig. 4.6a). This difference could be attributed to the weaker influence of the winter monsoon on the western slopes of the

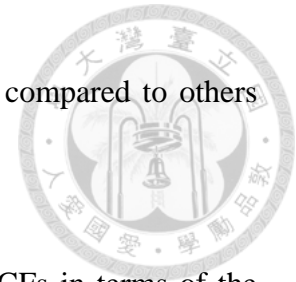


Central Mountain Range. Yet, further analysis of the seasonal variation of daytime RH in Western Taiwan is necessary to substantiate this speculation. Regarding the interannual variability of daytime RH, smaller variations in the MCF regions compared to other altitudes were also evident in Western Taiwan (Fig. 4.6b). However, the differences between the MCF areas and other regions were less pronounced in the west.

4.5 Vulnerable or resilient

The results of our study present a different perspective from previous studies that emphasized the vulnerability of MCFs. Previous research, such as RH simulations conducted by Still et al. (1999) in four MCFs worldwide, as well as observations of cloud base height and mist occurrence conducted by Pounds et al. (1999) in Monteverde, Costa Rica, and Williams et al. (2015) in coastal Southern California, have directly or indirectly suggested a decline in cloud and fog occurrence due to climate change, with negative impacts on MCFs. However, our analysis in Eastern Taiwan reveals contrasting findings. Despite the significant increase in both Q and Q_s , as expected under warming conditions, we found no significant trend in daytime RH from 1980 to 2021 in most of the analyzed regions, including the MCF areas. Furthermore, when considering the interannual variability of RH compared to higher and lower altitudes, we found that while RH tended to decrease during dry years across all elevations, the reduction was less pronounced in

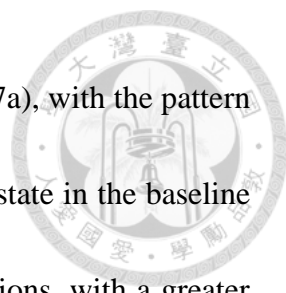
the MCFs, suggesting a relative resilience of RH in these regions compared to others during the studied period.



Our study does not directly address the vulnerability of the MCFs in terms of the impacts of warming and changes in rainfall patterns on montane cloud forest species. However, we speculate that if the resilience of RH reflects the persistence of cloud and fog occurrence, the presence of cloud and fog may serve as a mitigating factor for the extent of warming in MCFs by sustaining significant latent heat fluxes from the moist canopy. This potential mitigation mechanism could have positive implications for the conservation of endemic species in MCFs.

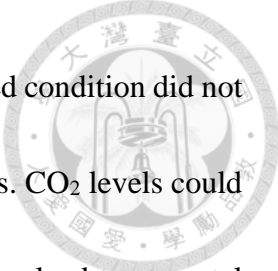
It is important to recognize that our findings regarding RH characteristics in Eastern Taiwan are based on the historical period from 1980 to 2021, and we cannot determine whether the unique RH patterns discovered in the MCF areas will persist under more intense climate changes. In order to gain insight into potential changes in RH under stronger warming scenarios, we analyzed another dataset provided by TCCIP that simulated a climate change scenario with 4K warming. This scenario used the years 2016-2020 from the TReAD data as the baseline and re-ran the model with a pseudo-global-warming (PGW) approach.

Fig. 4.7 illustrates the differences in mean daytime values between the 4K-enhanced scenario and the corresponding years (2016-2020) of the baseline. Under the 4K-



enhanced condition, both mean daytime Q and Q_s increased (Fig. 4.7a), with the pattern of increment along the altitude being similar to the pattern of mean state in the baseline (Fig. 3.1b). Daytime latent heat fluxes increased in all analyzed regions, with a greater variation of change in the low altitudes (Fig. 4.7b). However, the changes in daytime RH were generally less than 1.5% across all analyzed regions (Fig. 4.7c). Above 1500 m, daytime RH tended to decreased, while in low-altitude regions, RH changes displayed greater variability, including both increases and decreases. When examining the proportional increase relative to their mean state values in the baseline (Fig. 4.8a, b), both daytime Q and Q_s exhibited a greater extent of increase in the high altitudes. This can be attributed to the projected stronger warming in the high altitudes (Fig. 4.7d), which aligns with the observed and predicted rapid warming at high elevations reported in previous studies (Beniston et al., 1997; Foster, 2001; Pepin et al., 2022). Furthermore, in high altitudes, the extent of increase in Q_s was stronger than that of Q , leading to a greater decrease in daytime RH compared to mid- and low-altitude regions (Fig. 4.7c).

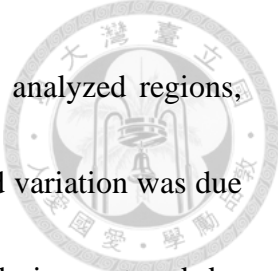
Indeed, the comparison of RH between the 4K-enhanced scenario and the baseline did not provide conclusive evidence for the upward shifting of the cloud-forming level. The minimal changes in RH can be attributed to the similar extent of increase in both Q and Q_s relative to their mean state values. Furthermore, the greater decrease in RH in the high altitudes compared to the MCFs contradicts the expected upward shift in high



daytime RH. However, it is important to consider that the 4K-enhanced condition did not account for the effects of increased CO₂ concentrations on vegetations. CO₂ levels could reach double or higher values in the 4K-enhanced scenario, which can lead to stomatal closure, reducing transpiration and causing a subsequent decrease in Q and RH. Another limitation in indicating the upward-shifting cloud-forming level is the use of mean RH values for all daytime hours as a direct representation of cloud and fog occurrence in a specific area. Variations in RH can differ even when mean values are similar. Moreover, fog occurrence at a particular moment depends on whether the current RH value surpasses a certain threshold. Therefore, it is possible that fog occurrence has undergone changes despite the similar mean RH values discovered in the non-significant daytime RH trend from 1980 to 2021 and the marginal difference between the 4K-enhanced and baseline scenarios.

Chapter 5 Conclusions

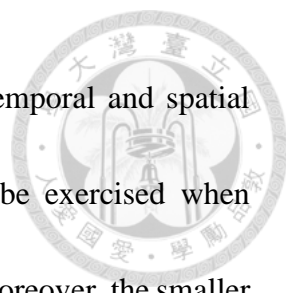
We summarize the unique microclimate characteristics and underlying mechanisms of Eastern Taiwan's MCFs in Fig. 4.1, highlighting the following primary findings: (1) the MCFs exhibited high daytime RH. The notable increase in RH after sunrise, compared to non-cloud-forested regions, was attributed to the substantial water vapor supply from local evapotranspiration and non-local transport. This high daytime RH was also influenced by the nonlinearity of the C-C relation with temperature; (2) Interannual



variations of daytime RH in the MCFs were smaller than in other analyzed regions, indicating a more stable interannual RH in the MCFs. This restrained variation was due to the energy-limited conditions that regulated water vapor supply during wet and dry years, as well as the relatively warmer temperatures in the MCFs compared to high-altitude regions.

The interannual variability of daytime RH across all altitudes demonstrated a higher level of resilience in Eastern Taiwan's MCFs in terms of RH, which contrasts with the vulnerability emphasized in previous studies. Our study underscores the importance of near-surface water vapor supply and moderate temperatures in shaping the unique RH characteristics in the MCFs, including both the mean state and interannual variations.

In our study, we acknowledge the omission of discussion regarding changes in non-local water vapor supply to the MCFs. Future research should strive to comprehensively understand the microclimate of these forests by quantifying the contribution of non-local water vapor sources and comparing them with local sources when examining mean state and interannual variations of water vapor within MCFs. It is also important to investigate how non-local water vapor sources in MCFs respond to changes in neighboring regions and the strength of mountain-valley winds under future climate scenarios. Furthermore, a series of experiments may be needed to attribute the primary cause of the unique RH features in these areas. In addition, we recognize that while the mean RH value can



provide insights into fog occurrence, it cannot directly represent temporal and spatial changes in cloud and fog occurrence. Therefore, caution should be exercised when interpreting the results and making comparisons with other studies. Moreover, the smaller interannual variations of daytime RH we discovered in Eastern Taiwan's MCFs may be specific to the time period of 1980-2021. Similarly, the data from the 4K-enhanced condition during 2016-2020 had limited duration for investigating changes in interannual variations of RH under the warming scenario and was derived based on pseudo global warming experiments. To assess the persistence of resilience in MCFs in the future, it is necessary to analyze data over an extended period, taking into account various climate factors and potential changes in environmental conditions.

FIGURES

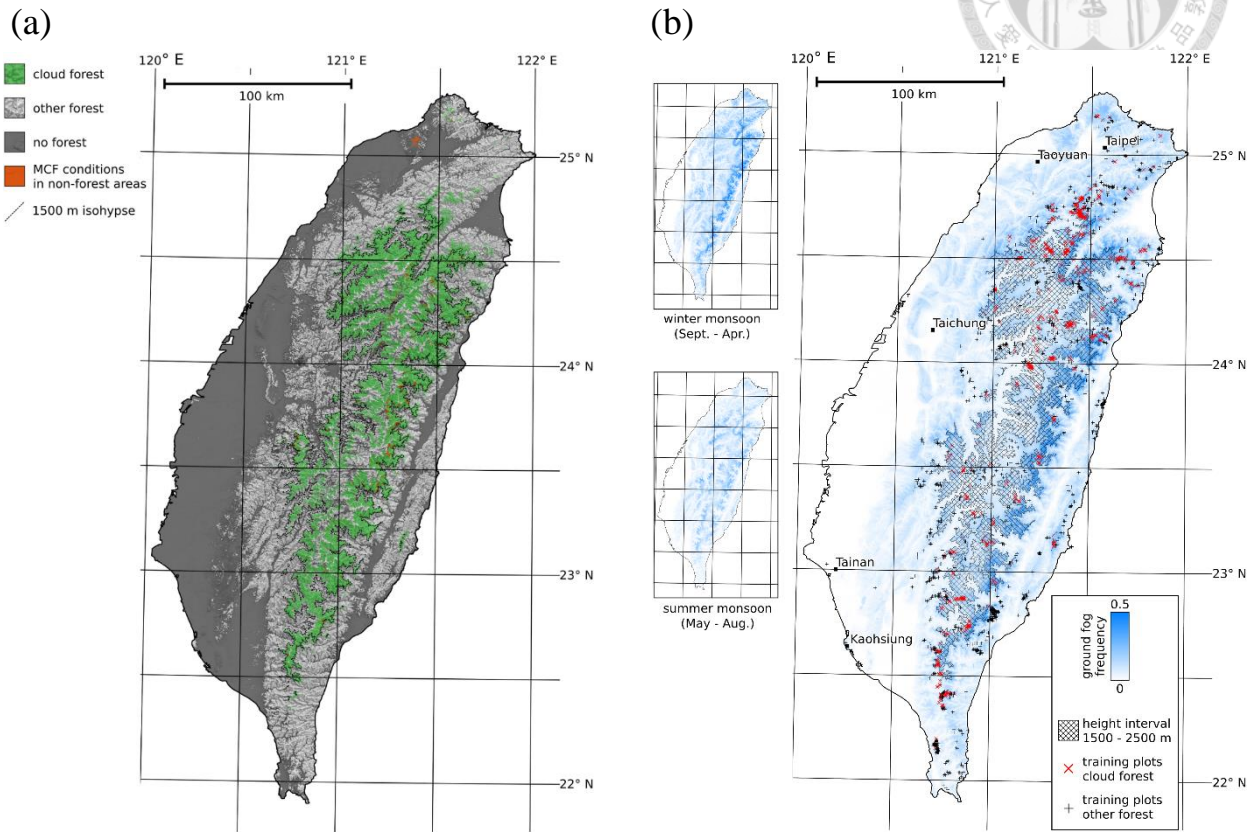


Figure 1. 1 (a) MCF distribution map of Taiwan, with the green area representing MCF areas. (b) Ground fog frequency map of Taiwan. (The figure is from Schulz et al. (2017).)

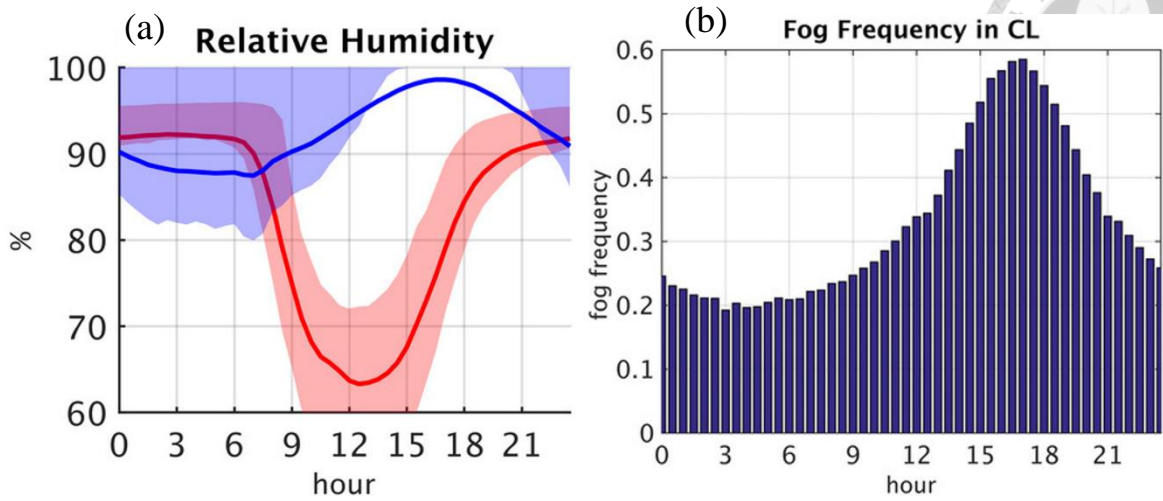


Figure 1. 2 (a) Diurnal cycle of relative humidity (% , as a unit) in Chi-Lan MCF (blue) and Lien-Hua-Chih noncloud forest (red). (b) The diurnal frequency of fog occurrence in Chi-Lan (CL) MCF. (The figure is from Gu et al. (2021).)

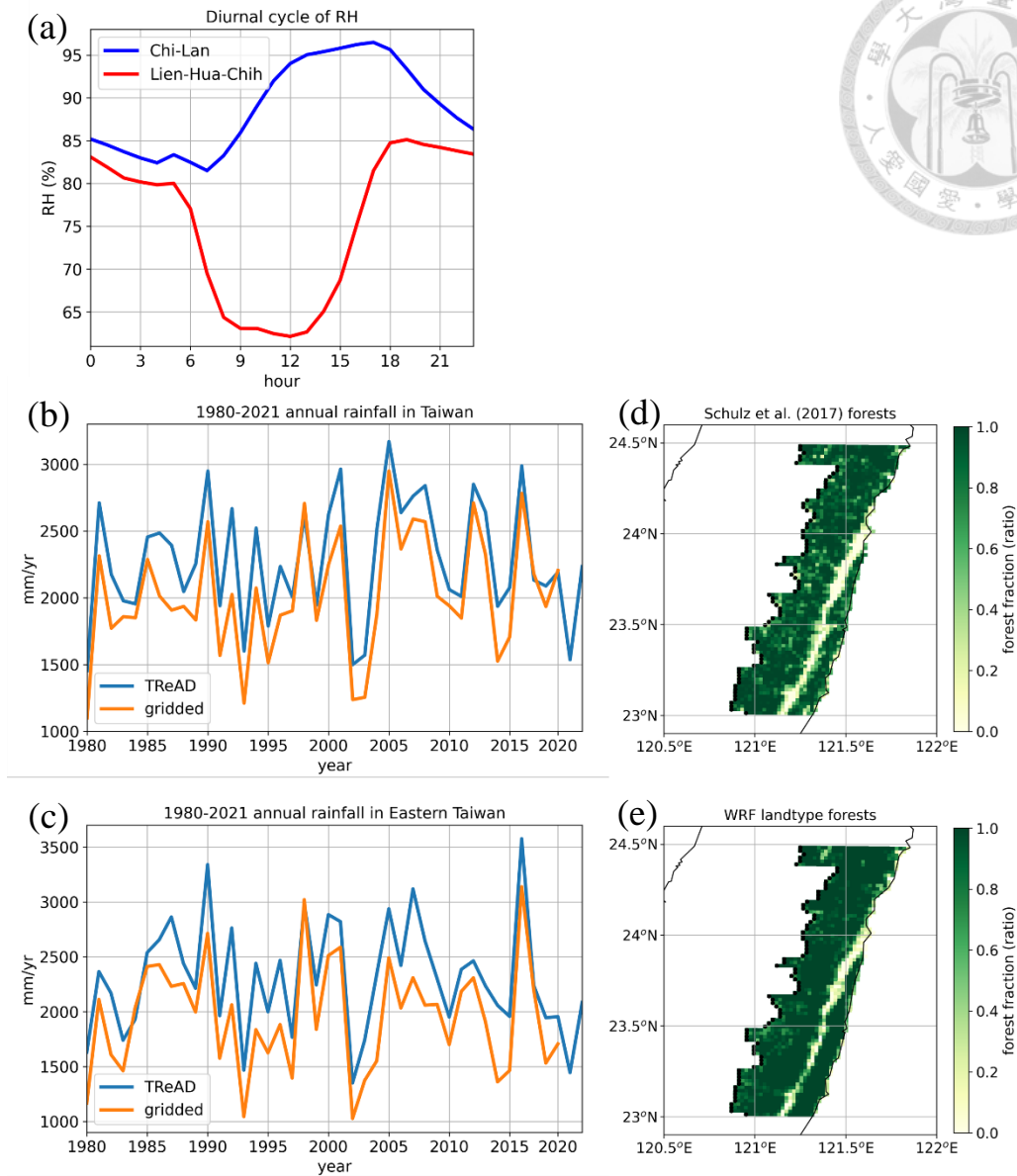


Figure 2. 1 Validation of TReAD data. (a) Diurnal cycle of relative humidity [RH (% , as a unit)] in the TReAD grid cell closest to Chi-Lan MCF (blue) and the TReAD grid cell closest to Lien-Hua-Chih noncloud forest (red). (b) Annual rainfall (mm/yr) in Taiwan obtained from TReAD data (blue) and gridded observational data (orange). (c) Annual rainfall (mm/yr) in Eastern Taiwan obtained from TReAD data (blue) and gridded observational data (orange). (d) Fraction of forests derived from the MCF distribution map provided by Schulz et al. (2017). (e) Fraction of forests derived from the land use and land cover map utilized in the TReAD downscaling process.

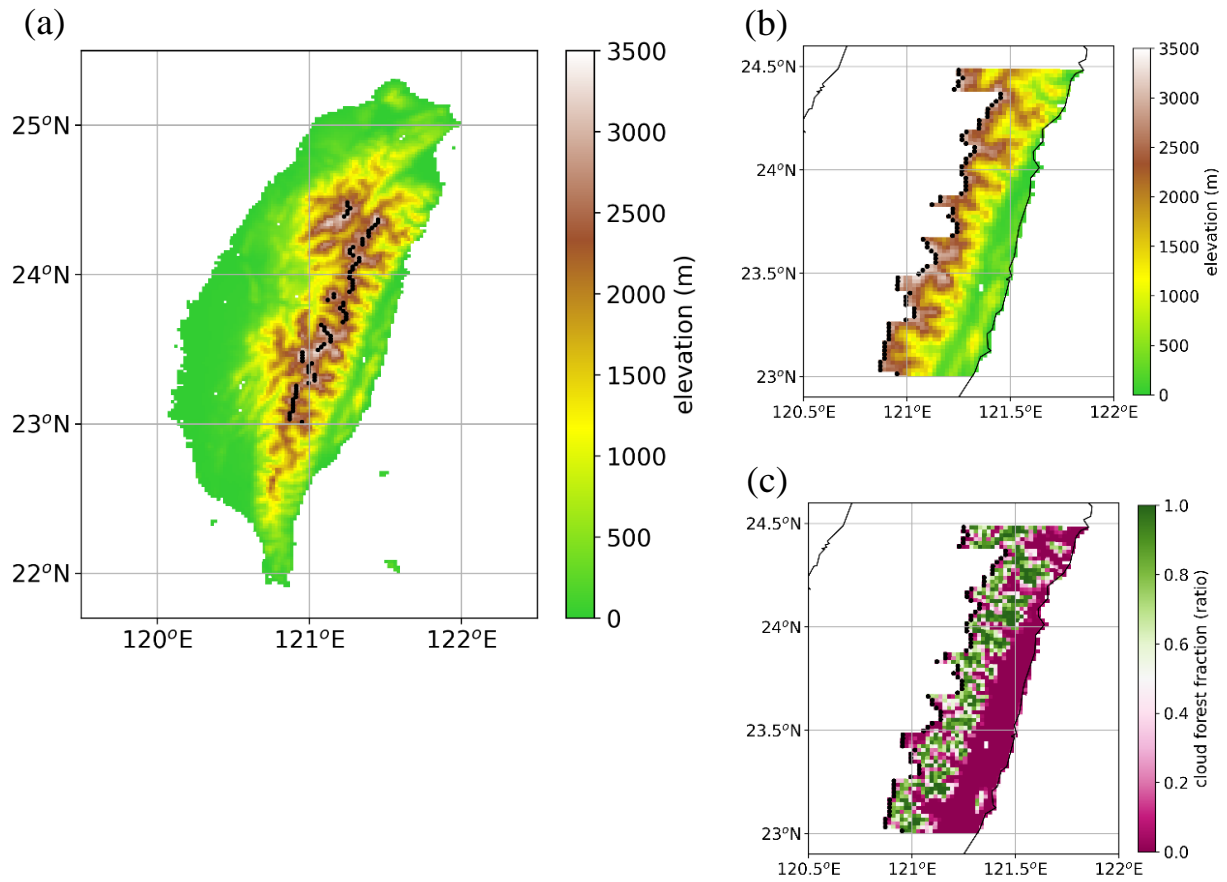


Figure 2. 2 The map of (a) topography in Taiwan, (b) topography in Eastern Taiwan, and (c) cloud forest fraction in Eastern Taiwan. Black dots are the highest grids in each latitude bounded between 23 and 24.5 degree North.

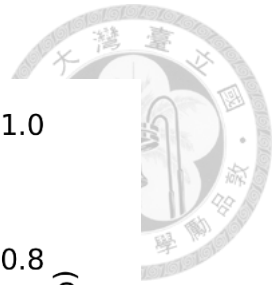
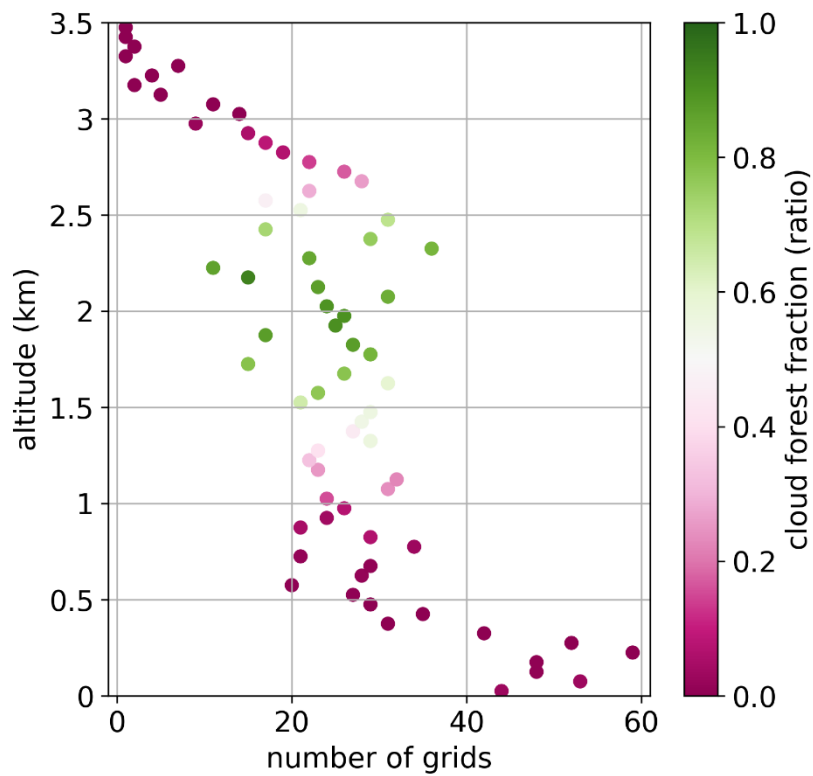


Figure 2. 3 Number of grids in each group separated by altitudes of every 50 m starting from an altitude of 0 m. Dots will be marked at the midpoint altitude of each group (e.g., the number of grids of 0 to 50 m will be plotted at an altitude of 25 m). Colors represent the cloud forest fraction averaged for each group, and the scale is the same as in Fig. 2.2c.

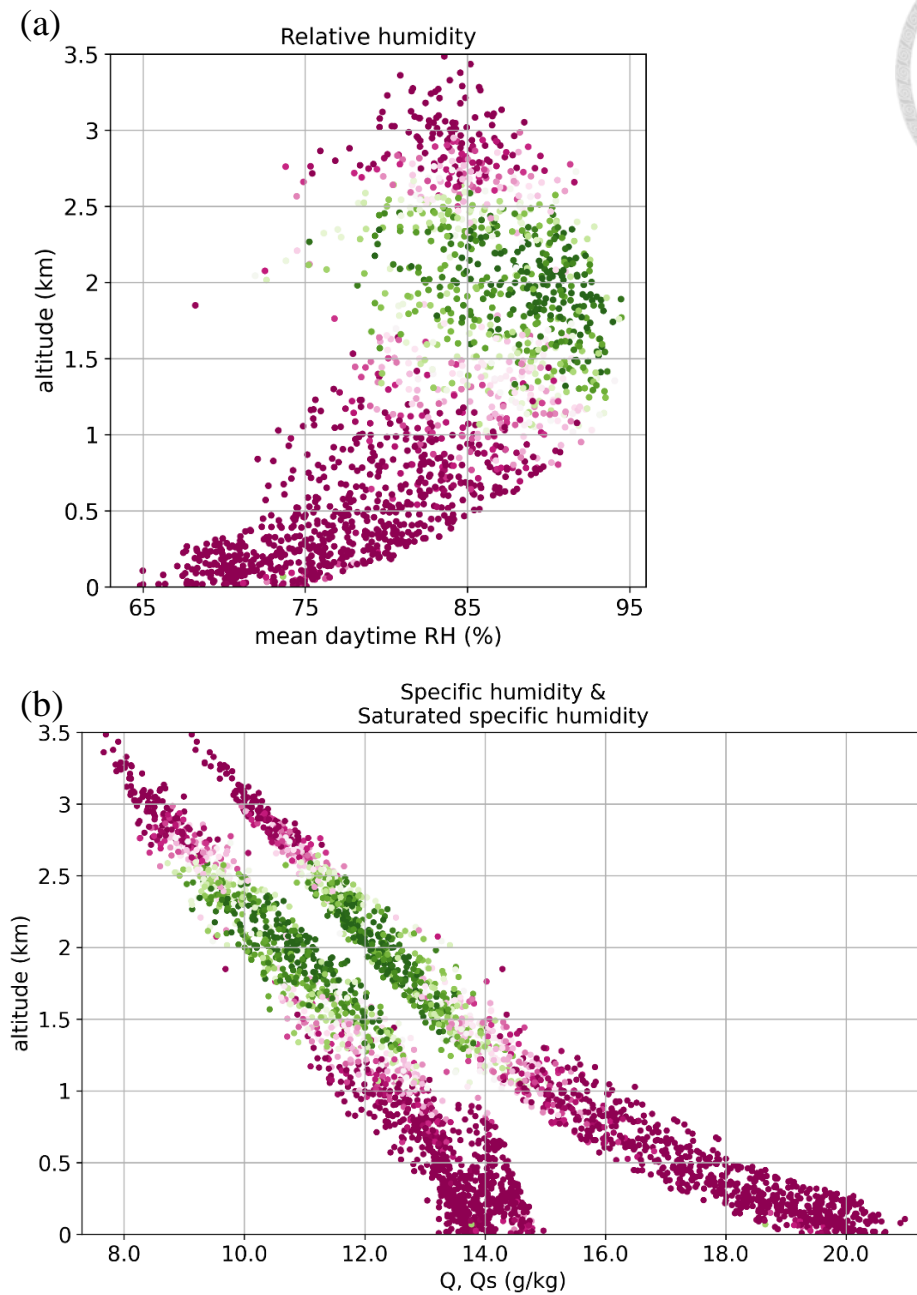


Figure 3. 1 (a) The relationship between mean daytime relative humidity [RH (% as a unit)] and altitude (km) in Eastern Taiwan. (b) The relationship between mean daytime specific humidity [Q (g/kg, pattern on the left)] and saturated specific humidity [Qs (g/kg, pattern on the right)] and altitude (km) in Eastern Taiwan. Each dot represents a grid. Colors represent the cloud forest fraction for each grid, and the scale is the same as in Fig. 2.2c.

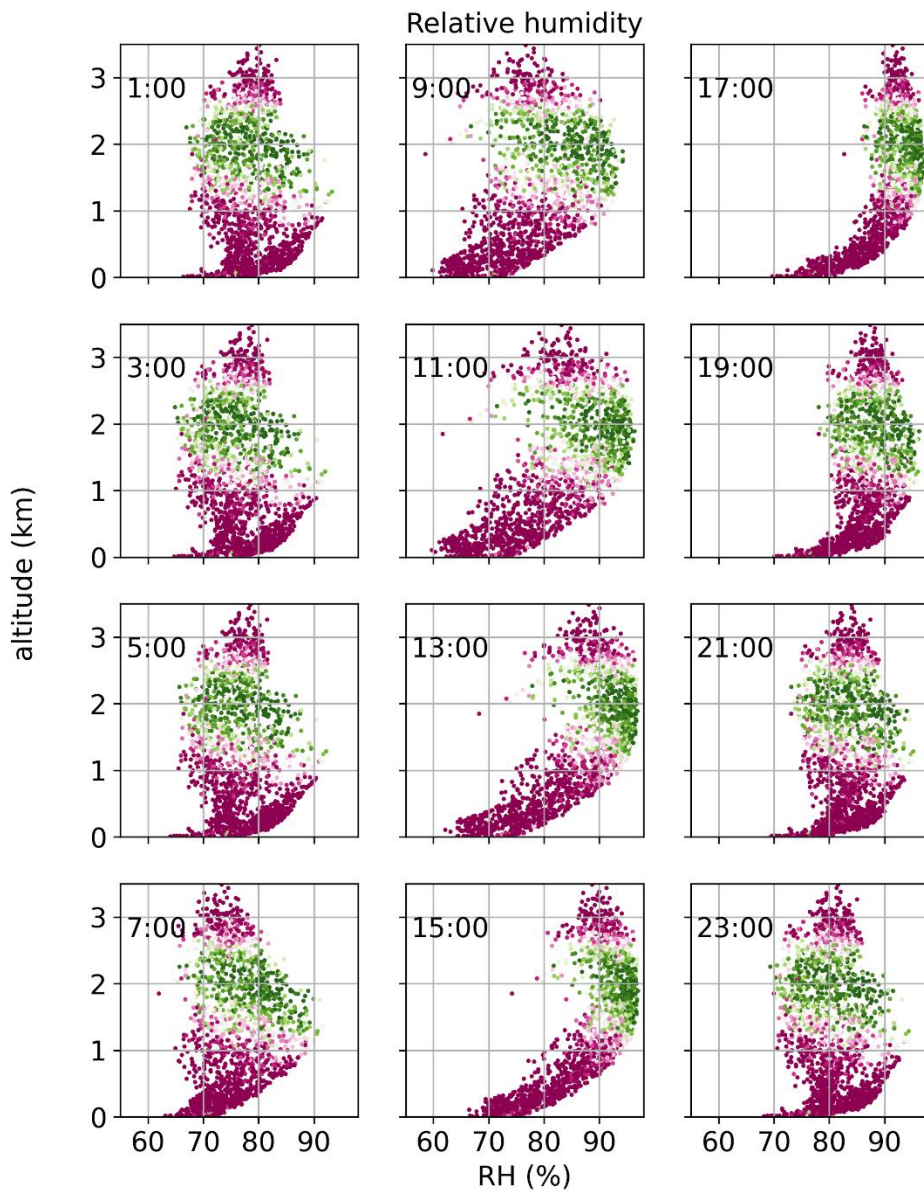


Figure 3. 2 Diurnal cycle of relative humidity [RH (% , as a unit)] along the altitude (km) in Eastern Taiwan. Local time is marked in the upper left of each subplot. Each dot represents a grid. Colors represent the cloud forest fraction for each grid, and the scale is the same as in Fig. 2.2c.

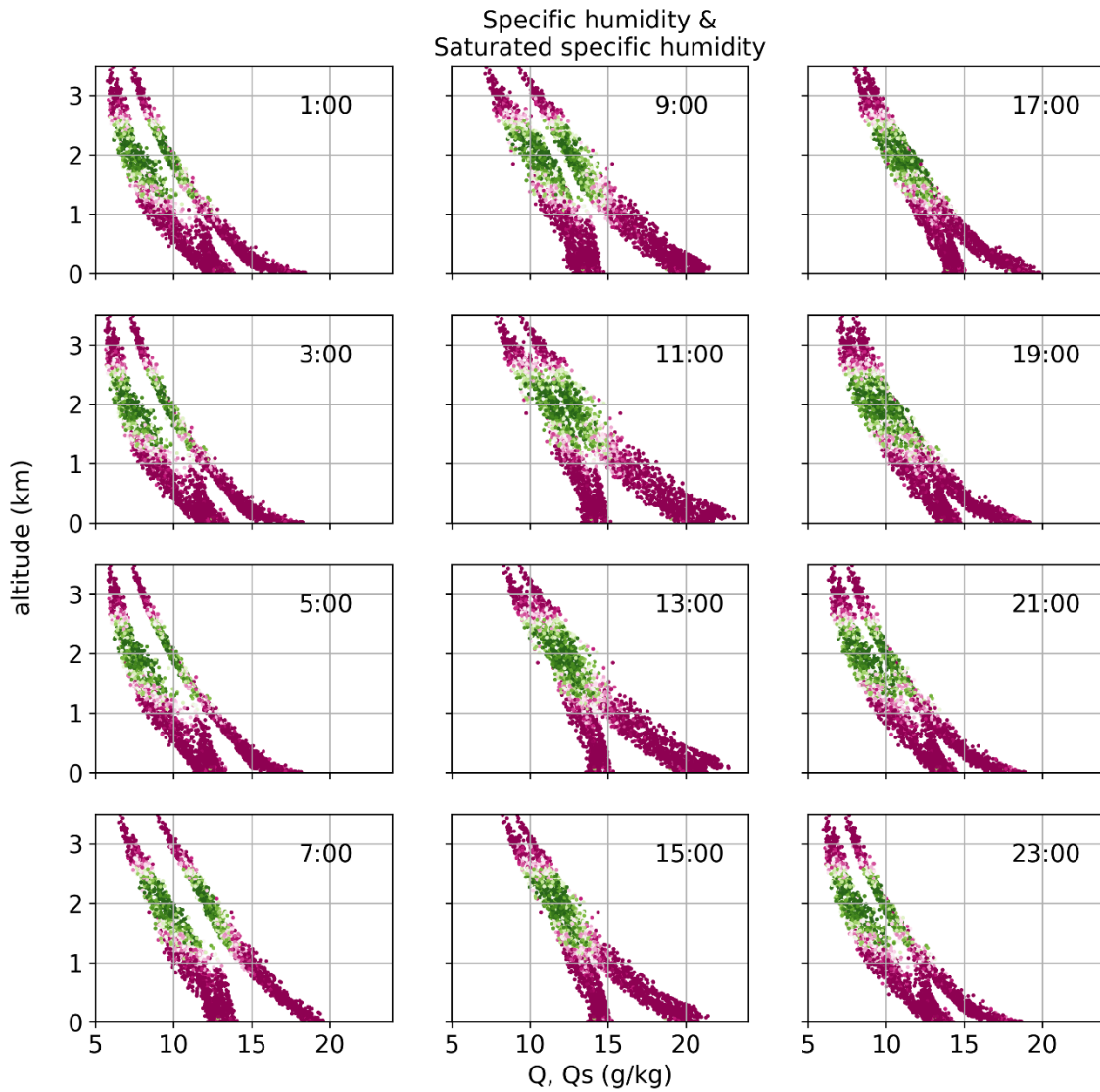


Figure 3.3 Diurnal cycle of specific humidity [Q (g/kg, patterns on the left of each panel)] and saturated specific humidity [Q_s (g/kg, patterns on the right of each panel)] along the altitude (km) in Eastern Taiwan. Local time is marked in the upper right of each panel. Each dot represents a grid. Colors represent the cloud forest fraction for each grid, and the scale is the same as in Fig. 2.2c.

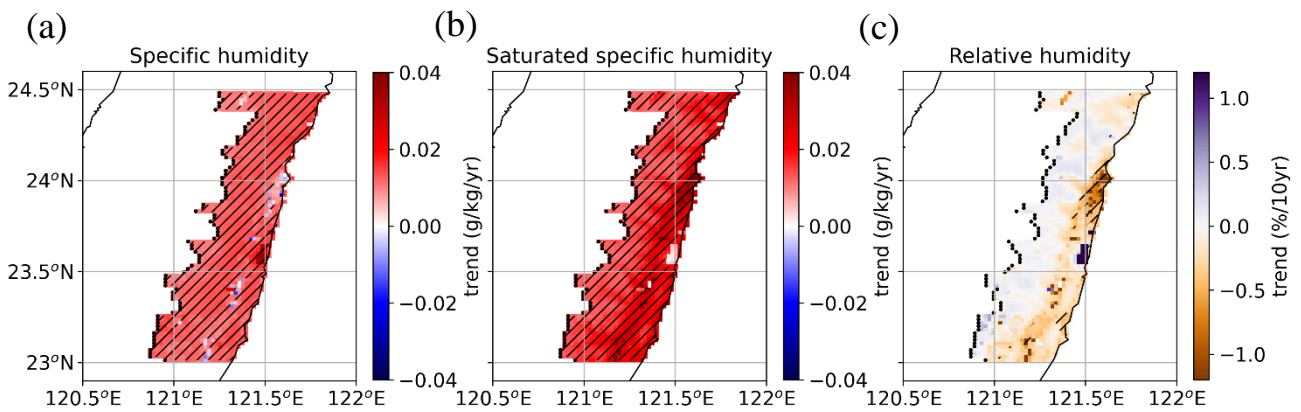


Figure 3. 4 Trends of daytime (a) specific humidity, (b) saturated specific humidity, and (c) relative humidity during 1980-2021 in Eastern Taiwan. Hatched areas have significant trends (p -value < 0.05). Trends are calculated using annual values, but values of relative humidity trend are multiplied by 10 when plotting the colorbar.

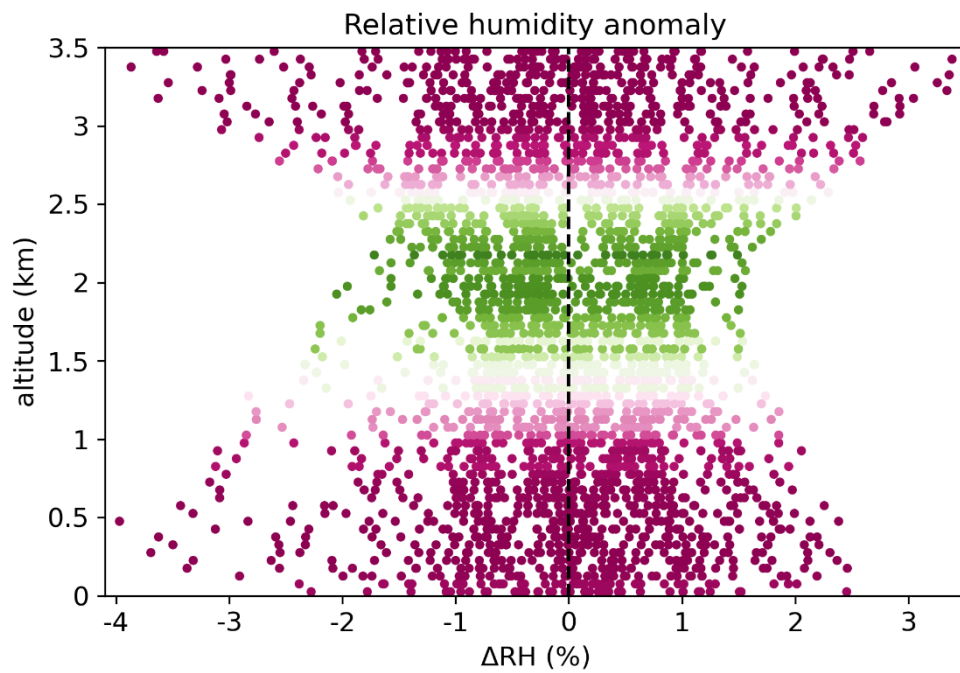


Figure 3. 5 Anomalies of daytime relative humidity [RH (%), as a unit] along the altitude (km) for each year in 1980-2021 in Eastern Taiwan. Each dot represents the anomaly of each year compared to 42-year mean in each group. Colors represent the cloud forest fraction averaged for each group, and the scale is the same as in Fig. 2.2c.

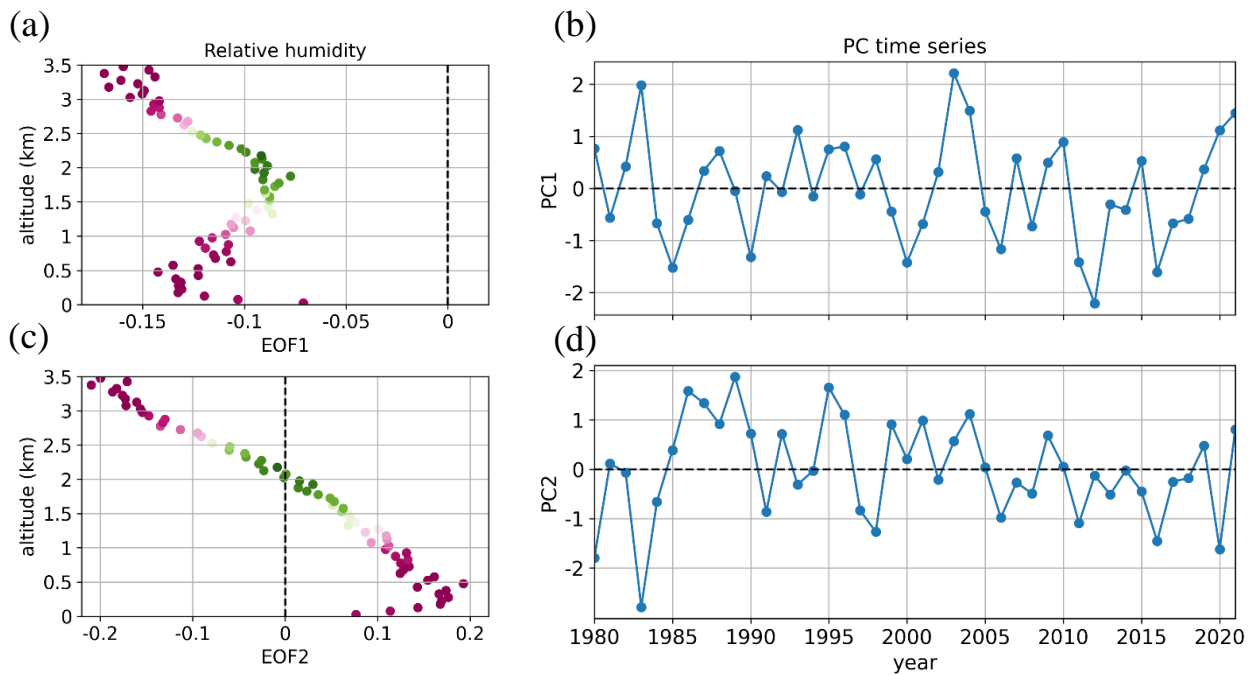


Figure 3. 6 (a, b) Mode 1 and (c, d) mode 2 of the EOF analysis on the anomalies of daytime relative humidity along the altitude for each year in 1980-2021. (a) and (c) are the vertical spatial distributions (EOFs); Colors represent the cloud forest fraction averaged for each group, and the scale is the same as in Fig. 2.2c. (b) and (d) are the time coefficients (PCs).

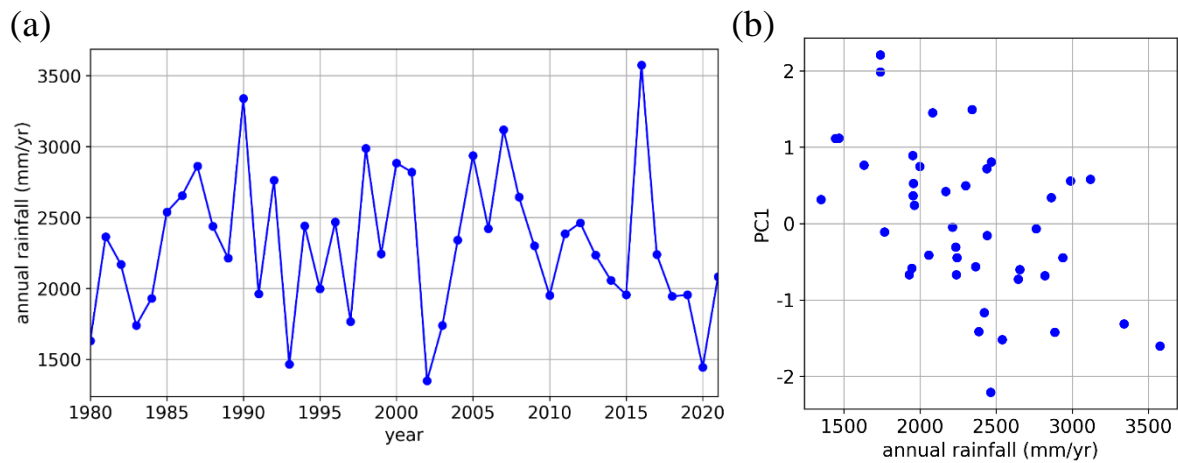


Figure 3. 7 (a) Annual rainfall (mm/yr) in Eastern Taiwan during 1980-2021. (b) The relationship between annual rainfall (mm/yr) in Eastern Taiwan and the time coefficients of mode 1 (PC1) of the EOF analysis on the anomalies of daytime relative humidity along the altitude during 1980-2021.

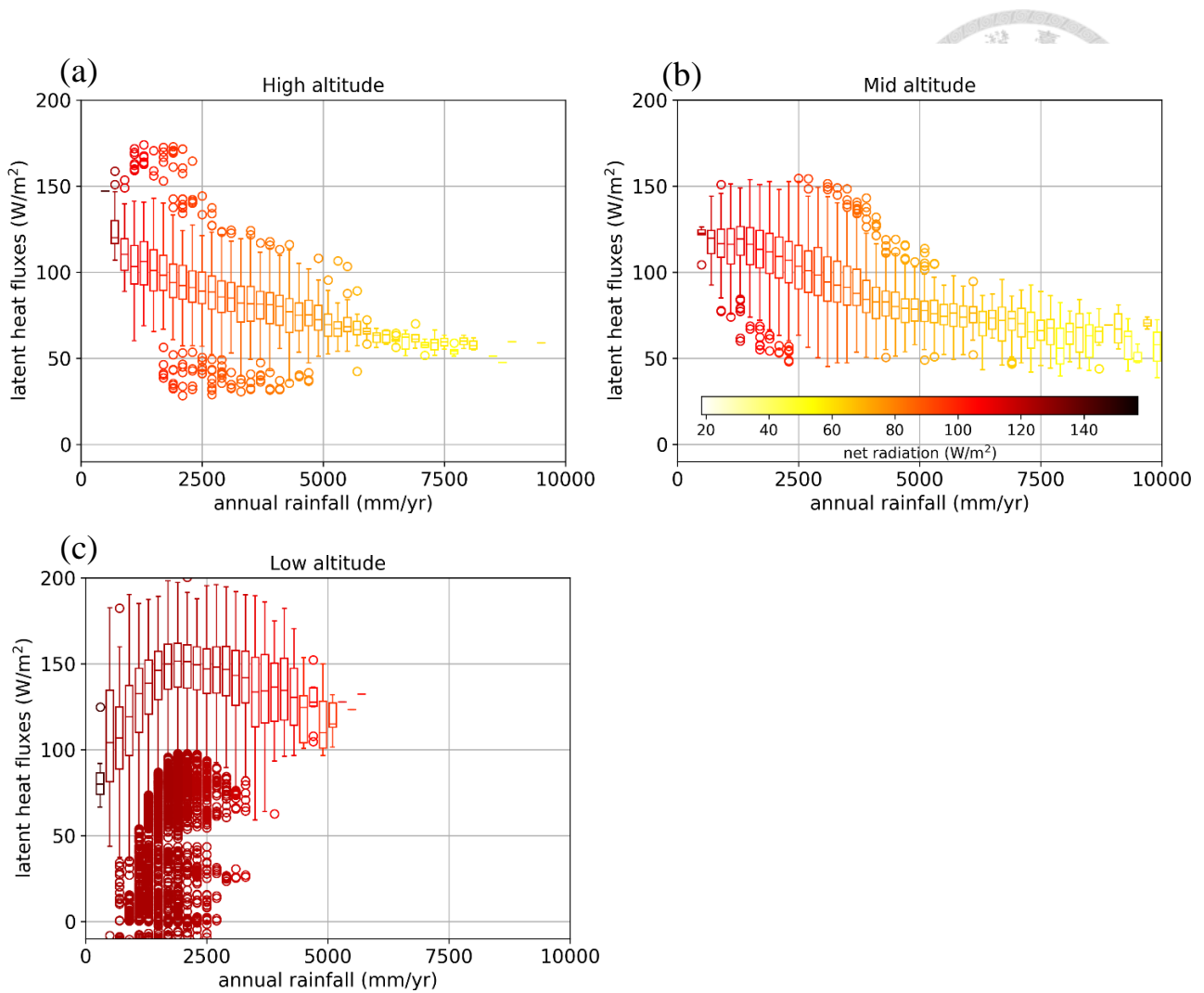


Figure 3. 8 The relationship between annual rainfall (mm/yr) and annual mean daytime latent heat fluxes (W/m²) in (a) high altitude, (b) mid altitude, and (c) low altitude (only grids with cloud forest fraction > 0.9 are presented in mid altitude and only grids with cloud forest fraction < 0.1 are presented in high and low altitude). Years and grids are grouped by every 200 mm/yr of rainfall to produce the boxplots. Colors represent the annual mean net radiation (W/m²) for the average of each group, and the colorbar in (b) fits every panel. Negative values of latent heat fluxes result from the detrending process on grids experiencing land use changes.

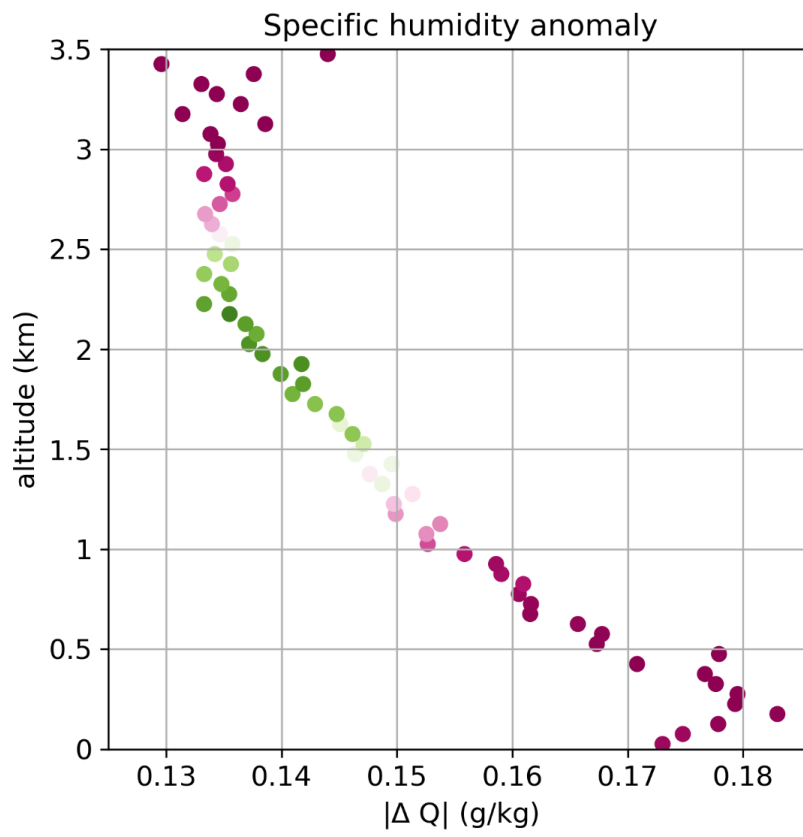


Figure 3. 9 The averaged absolute differences of daytime specific humidity [Q (g/kg)] to the local climatology along the altitude (km). Colors represent the cloud forest fraction averaged for each group, and the scale is the same as in Fig. 2.2c.

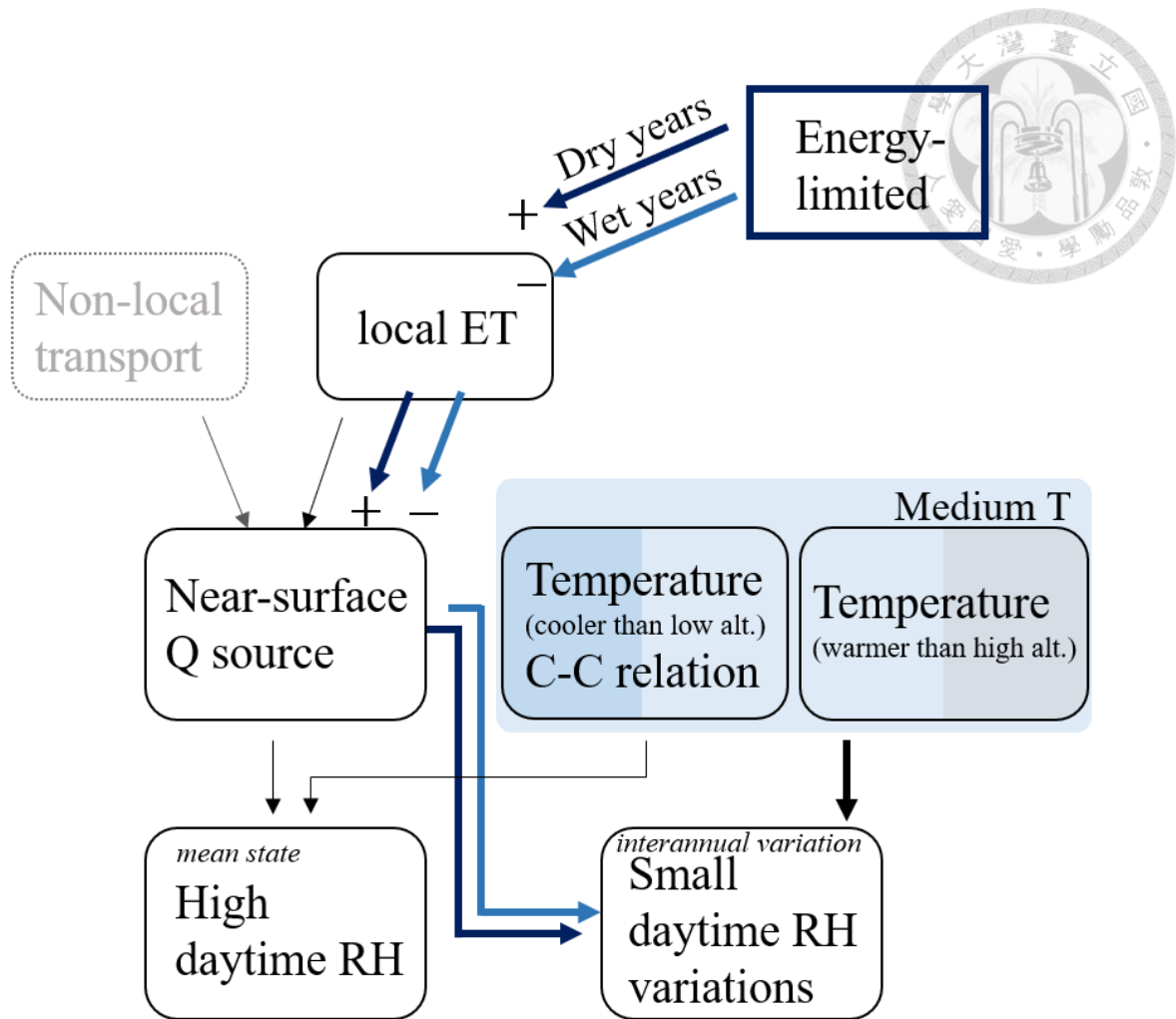


Figure 4. 1 Schematic plot of mechanisms behind high daytime relative humidity [RH] and small daytime RH variations in Eastern Taiwan's MCF areas. Thin (thick) arrows refer to mechanisms related to mean state (interannual variation) of RH. + (-) represents increase (decrease) of the pointed term. ET stands for evapotranspiration and T stands for temperature. Color of box regarding non-local transport is lightened as our analysis didn't focus on its change.

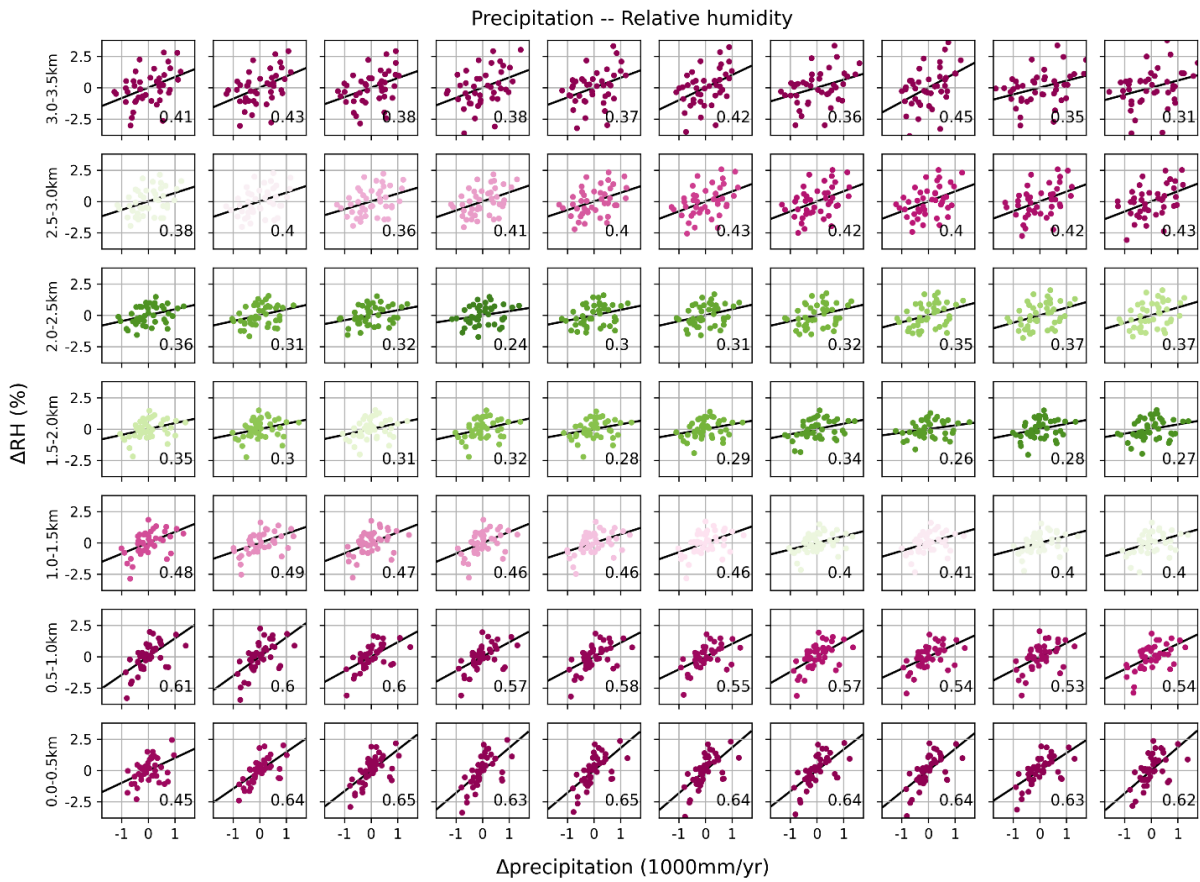


Figure 4. 2 The relationship between annual precipitation (mm/yr) and relative humidity [RH (% , as a unit)] in each group. The panels progress from the lowest elevation in the bottom left to the highest elevation in the top right. Values of precipitation and RH are the anomalies compared to local climatology. Black lines are the linear fitting for the relation in each group, and the correlation coefficients for the linear fitting are shown in the lower right of each panel. Colors represent the cloud forest fraction averaged for each group, and the scale is the same as in Fig. 2.2c.

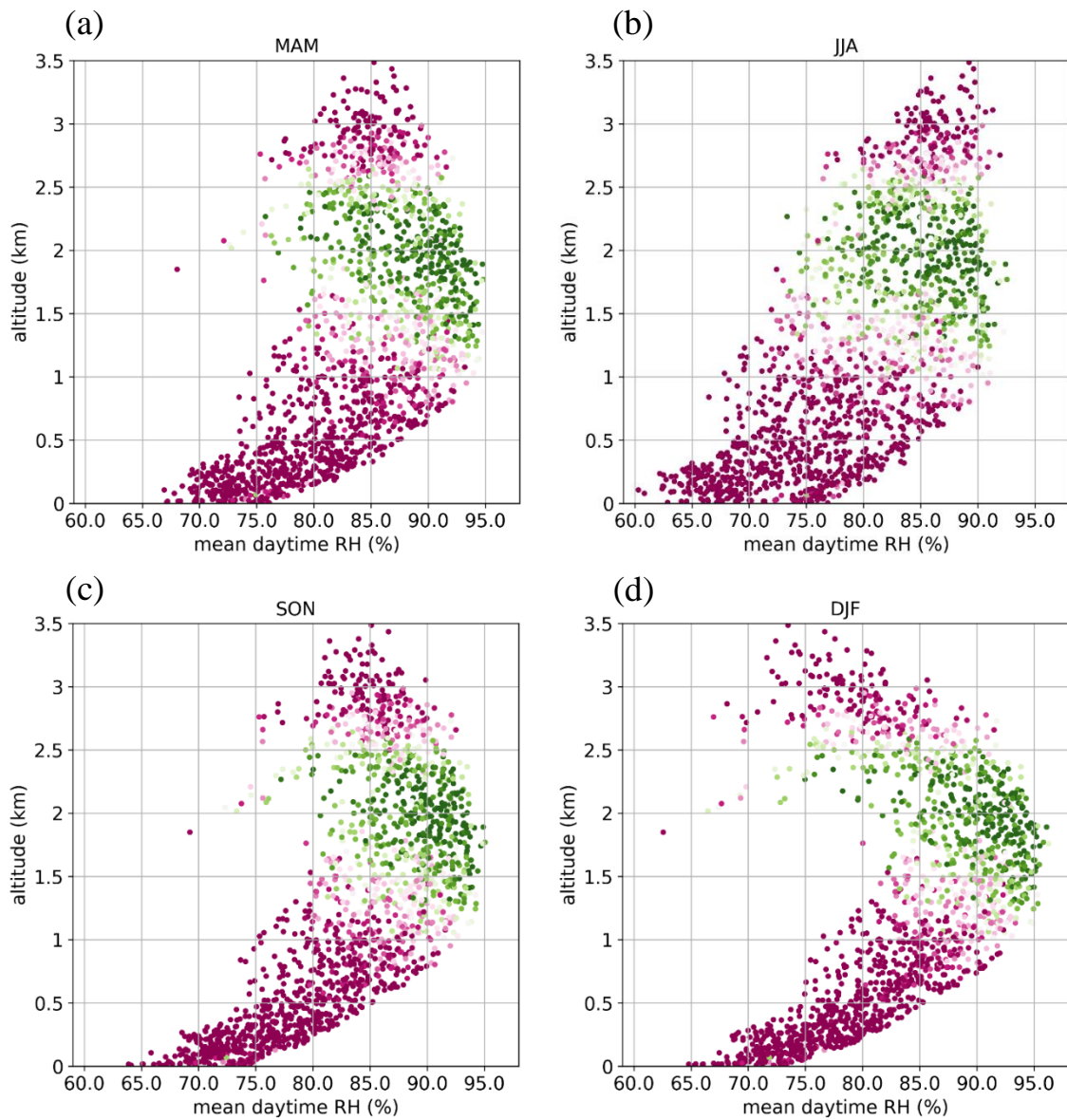


Figure 4. 3 The relationship between mean daytime relative humidity [RH (%), as a unit] and altitude (km) in Eastern Taiwan in (a) spring (March-May, MAM), (b) summer (June-August, JJA), (c) autumn (September-November, SON), and (d) winter (December-February, DJF). Each dot represents a grid. Colors represent the cloud forest fraction for each grid, and the scale is the same as in Fig. 2.2c.

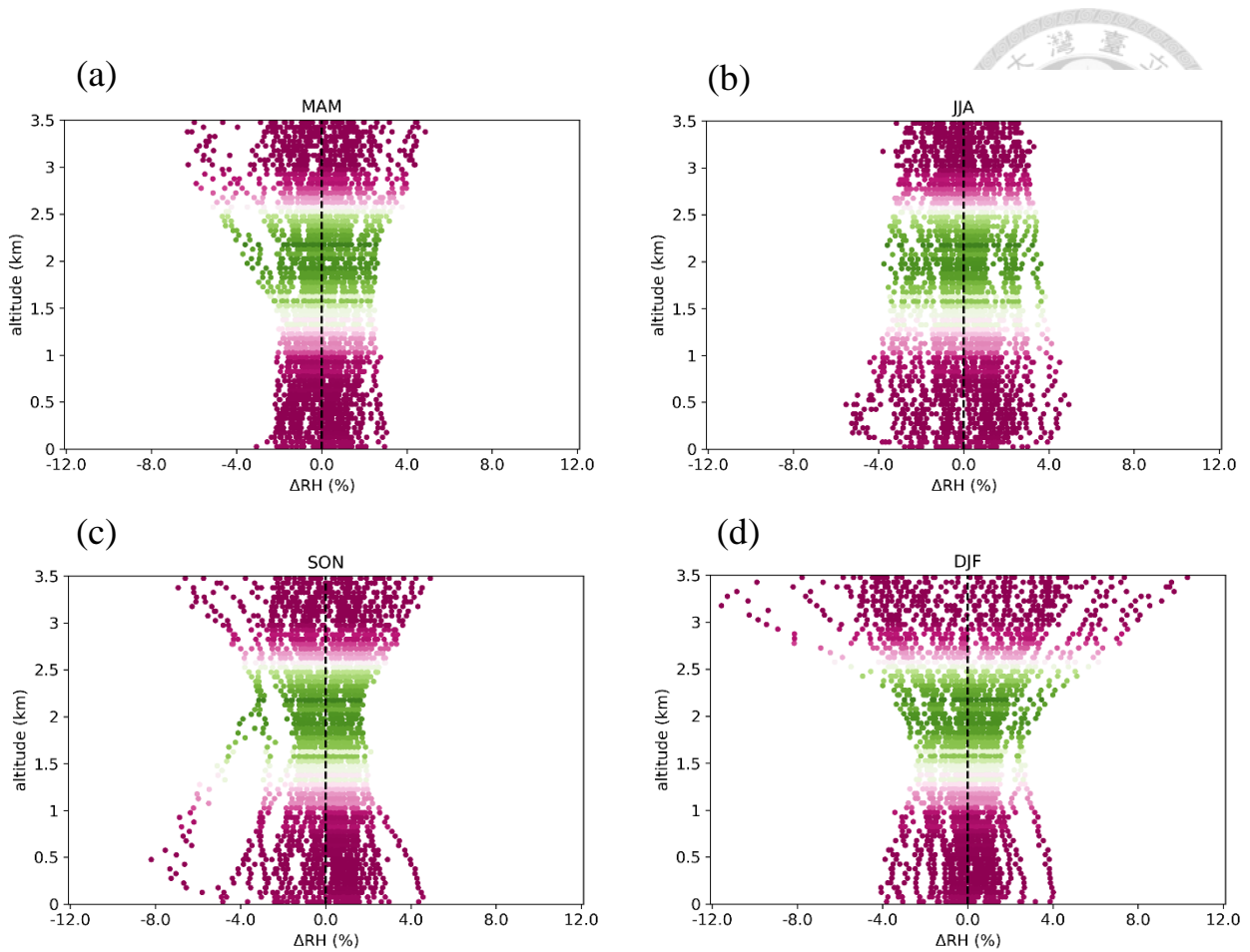


Figure 4. 4 Anomalies of daytime relative humidity [RH (% , as a unit)] along the altitude (km) in (a) spring (March-May, MAM), (b) summer (June-August, JJA), (c) autumn (September-November, SON), and (d) winter (December-February, DJF) for each year in 1980-2021. Each dot represents the anomaly of each year compared to 42-year mean in each group. Colors represent the cloud forest fraction averaged for each group, and the scale is the same as in Fig. 2.2c.

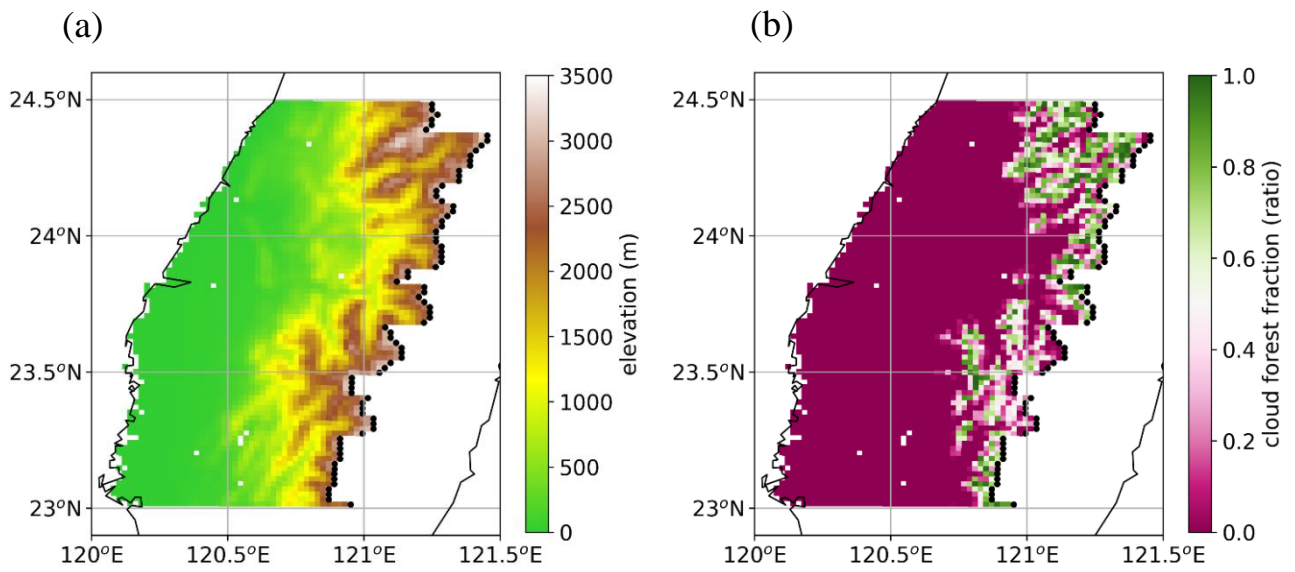


Figure 4. 5 The map of (a) topography and (b) cloud forest fraction in Western Taiwan. Black dots are the highest grids in each latitude bounded between 23 and 24.5 degree North.

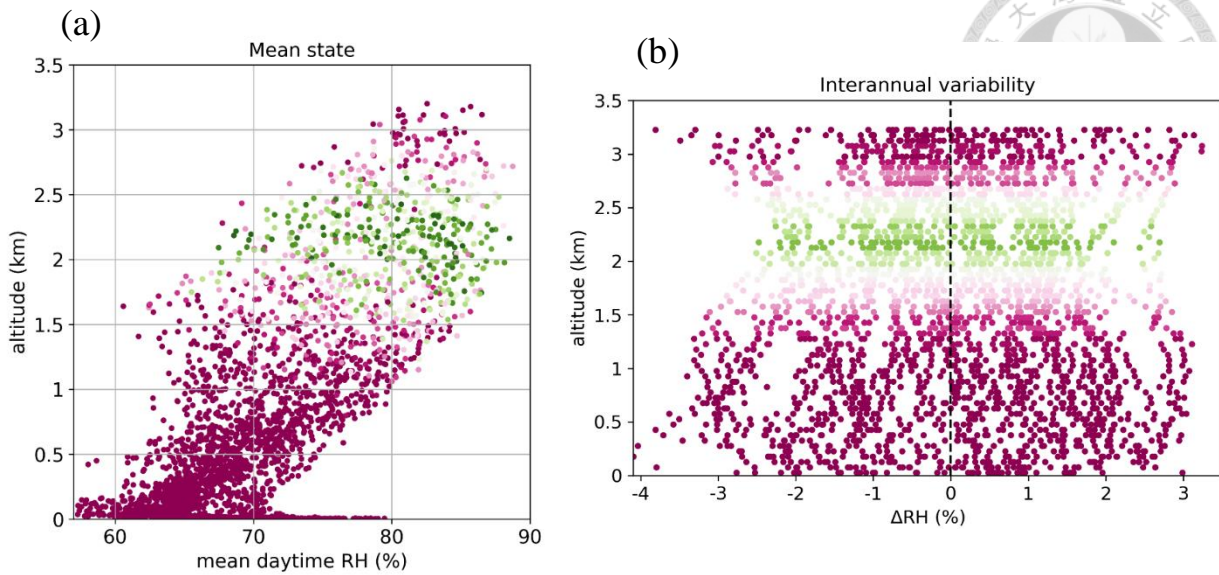


Figure 4. 6 (a) The relationship between mean daytime relative humidity [RH (% , as a unit)] and altitude (km) in Western Taiwan. Each dot represents a grid. Colors represent the cloud forest fraction for each grid. (b) Anomalies of daytime relative humidity [RH (% , as a unit)] along the altitude (km) for each year in 1980-2021 in Western Taiwan. Each dot represents the anomaly of each year compared to 42-year mean in each group. Colors represent the cloud forest fraction averaged for each group. The scale of colors in (a) and (b) are the same as in Fig. 2.2c.

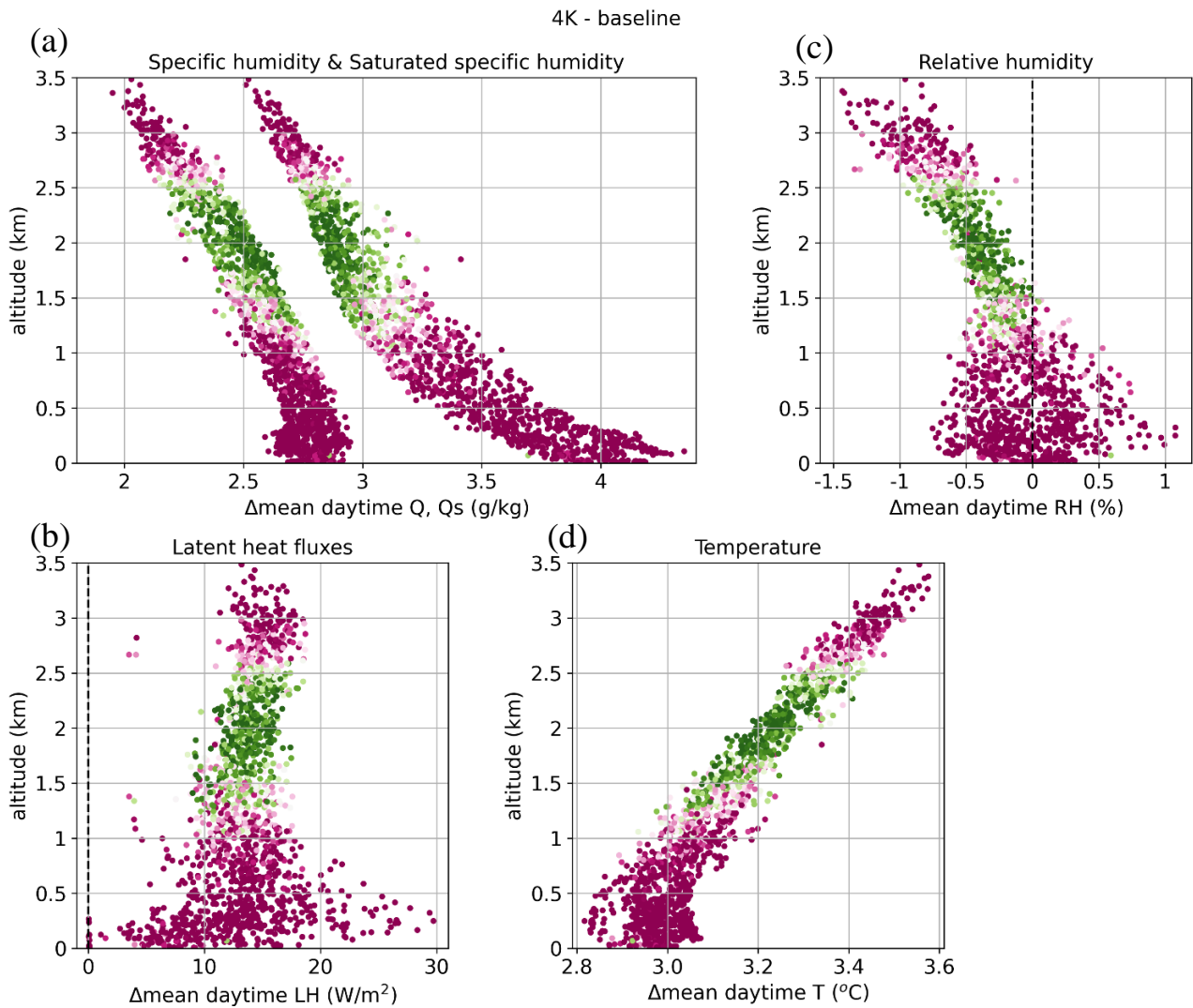


Figure 4. 7 Differences of mean daytime values of 5 meteorological variables between the 4K-enhanced scenario (4K) and baseline in Eastern Taiwan: (a) specific humidity [Q (g/kg, pattern on the left)] and saturated specific humidity [Qs (g/kg, pattern on the right)], (b) latent heat fluxes [LH (W/m^2)], (c) relative humidity [RH (%), as a unit], and (d) temperature [T ($^{\circ}\text{C}$)]. Each dot represents a grid. Colors represent the cloud forest fraction for each grid, and the scale is the same as in Fig. 2.2c.

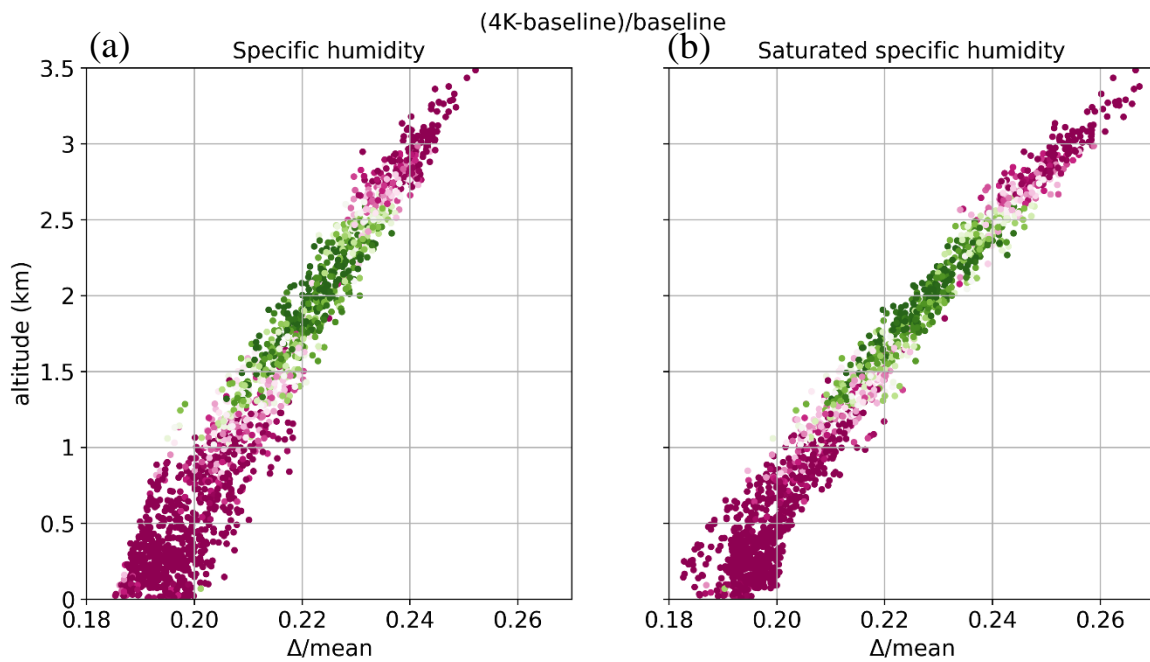


Figure 4. 8 Proportional increase of (a) specific humidity and (b) saturated specific humidity from baseline to the 4K-enhanced scenario (4K) relative to their mean state values in the baseline. Each dot represents a grid. Colors represent the cloud forest fraction for each grid, and the scale is the same as in Fig. 2.2c.

REFERENCES



林秉毅、鄭兆尊、陳永明、簡毓瑋 (2021)。40 年高解析度臺灣歷史氣候資料。國家災害防救科技中心。

Beniston, M., Diaz, H. F., & Bradley, R. S. (1997). Climatic change at high elevation sites: an overview. *Climatic Change*, 36(3-4), 233–251.
<https://doi.org/10.1023/A:1005380714349>

Bruijnzeel, L. A., Mulligan, M., & Scatena, F. N. (2011). Hydrometeorology of tropical montane cloud forests: emerging patterns. *Hydrological Processes*, 25(3), 465-498.
<https://doi.org/10.1002/hyp.7974>

Bruijnzeel, L. A., Scatena, F. N., & Hamilton, L. S. (Eds.). (2011). *Tropical montane cloud forests: science for conservation and management*. Cambridge University Press.

Bubb, P., May, I., Miles, L., & Sayer, J. (2004). *Cloud forest agenda*. UNEP-WCMC, Cambridge, UK.

Chang, S. C., Lai, I. L., & Wu, J. T. (2002). Estimation of fog deposition on epiphytic bryophytes in a subtropical montane forest ecosystem in northeastern Taiwan. *Atmospheric Research*, 64(1-4), 159-167. [https://doi.org/10.1016/S0169-8095\(02\)00088-1](https://doi.org/10.1016/S0169-8095(02)00088-1)



Chen, F. (2007, April). The Noah land surface model in WRF: a short tutorial. In *LSM group meeting*.

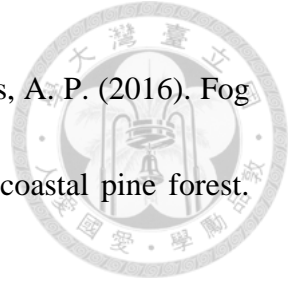
Chen, Y. Y., Huang, W., Wang, W. H., Juang, J. Y., Hong, J. S., Kato, T., & Luysaert, S. (2019). Reconstructing Taiwan's land cover changes between 1904 and 2015 from historical maps and satellite images. *Scientific reports*, 9(1), 3643. <https://doi.org/10.1038/s41598-019-40063-1>

Chu, H. S., Chang, S. C., Klemm, O., Lai, C. W., Lin, Y. Z., Wu, C. C., Lin, J. Y., Jiang, J. Y., Chen, J., Gottgens, J. F., & Hsia, Y. J. (2014). Does canopy wetness matter? Evapotranspiration from a subtropical montane cloud forest in Taiwan. *Hydrological Processes*, 28(3), 1190-1214. <https://doi.org/10.1002/hyp.9662>

Danielson, J. J., & Gesch, D. B. (2011). *Global multi-resolution terrain elevation data 2010 (GMTED2010)*. U.S. Geological Survey. <https://doi.org/10.3133/ofr20111073>

Dawson, A. (2016). eofs: A Library for EOF Analysis of Meteorological, Oceanographic, and Climate Data. *Journal of Open Research Software*, 4(1), p.e14. <https://doi.org/10.5334/jors.122>

European Centre for Medium-Range Weather Forecasts. (2017). *ERA5 Reanalysis* (Updated monthly) [Data set]. Research Data Archive at the National Center for Atmospheric Research, Computational and Information Systems Laboratory. <https://doi.org/10.5065/D6X34W69>.



Fischer, D. T., Still, C. J., Ebert, C. M., Baguskas, S. A., & Williams, A. P. (2016). Fog drip maintains dry season ecological function in a California coastal pine forest.

Ecosphere, 7(6), e01364. <https://doi.org/10.1002/ecs2.1364>

Forzieri, G., Miralles, D. G., Ciais, P., Alkama, R., Ryu, Y., Duveiller, G., Zhang, K.,

Robertson, E., Kautz, M., Martens, B., Jiang, C., Arneth, A., Georgievski, G., Li,

W., Ceccherini, G., Anthoni, P., Lawrence, P., Wiltshire, A., Pongratz, J., ... &

Cescatti, A. (2020). Increased control of vegetation on global terrestrial energy

fluxes. *Nature Climate Change*, 10(4), 356-362. [https://doi.org/10.1038/s41558-](https://doi.org/10.1038/s41558-020-0717-0)

[020-0717-0](https://doi.org/10.1038/s41558-020-0717-0)

Foster, P. (2001). The potential negative impacts of global climate change on tropical

montane cloud forests. *Earth-Science Reviews*, 55(1-2), 73-106.

[https://doi.org/10.1016/S0012-8252\(01\)00056-3](https://doi.org/10.1016/S0012-8252(01)00056-3)

Grubb, P.J. (1977). Control of forest growth and distribution on wet tropical mountains:

with special reference to mineral nutrition. *Annual Review of Ecology and*

Systematics, 8(1), 83-107.

Gu, R. Y., Lo, M. H., Liao, C. Y., Jang, Y. S., Juang, J. Y., Huang, C. Y., Chang, S. C.,

Hsieh, C. I., Chen, Y. Y., Chu, H., & Chang, K. Y. (2021). Early peak of latent heat

fluxes regulates diurnal temperature range in montane cloud forests. *Journal of*

Hydrometeorology, 22(9), 2475-2487. <https://doi.org/10.1175/JHM-D-21-0005.1>



Hamilton, L. S., Juvik, J.O., & Scatena, F. N. (1993). Tropical montane cloud forests: proceedings of an international symposium at San Juan, Puerto Rico, 31 May-5 June 1993.

Kayaba, N., Yamada, T., Hayashi, S., Onogi, K., Kobayashi, S., Yoshimoto, K., Kamiguchi, K., & Yamashita, K. (2016). Dynamical regional downscaling using the JRA-55 reanalysis (DSJRA-55). *Sola*, 12, 1-5. <https://doi.org/10.2151/sola.2016-001>

Lai, G. Y., Liu, H. C., Chung, C. H., Wang, C. K., & Huang, C. Y. (2021). Lidar-derived environmental drivers of epiphytic bryophyte biomass in tropical montane cloud forests. *Remote Sensing of Environment*, 253, 112166. <https://doi.org/10.1016/j.rse.2020.112166>

Mata-Guel, E. O., Soh, M. C. K., Butler, C. W., Morris, R. J., Razgour, O., & Peh, K. S.-H. (2023). Impacts of anthropogenic climate change on tropical montane forests: an appraisal of the evidence. *Biological Reviews*, 98, 1200-1224. <https://doi.org/10.1111/brv.12950>

Mildenberger, K., Beiderwieden, E., Hsia, Y. J., & Klemm, O. (2009). CO₂ and water vapor fluxes above a subtropical mountain cloud forest—The effect of light conditions and fog. *Agricultural and Forest Meteorology*, 149(10), 1730-1736. <https://doi.org/10.1016/j.agrformet.2009.06.004>

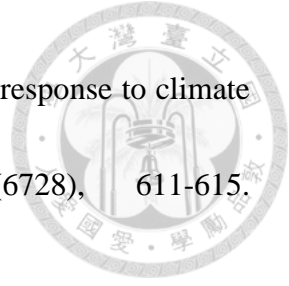


Nair, U. S., Lawton, R. O., Welch, R. M., & Pielke, R. A. (2003). Impact of land use on Costa Rican tropical montane cloud forests: Sensitivity of cumulus cloud field characteristics to lowland deforestation. *Journal of Geophysical Research: Atmospheres*, *108*(D7), 4206. <https://doi.org/10.1029/2001JD001135>

Oliveira, R. S., Eller, C. B., Bittencourt, P. R., & Mulligan, M. (2014). The hydroclimatic and ecophysiological basis of cloud forest distributions under current and projected climates. *Annals of Botany*, *113*(6), 909-920. <https://doi.org/10.1093/aob/mcu060>

Pauchard, A., Kueffer, C., Dietz, H., Daehler, C. C., Alexander, J., Edwards, P. J., Arévalo, J. R., Cavieres, L. A., Guisan, A., Haider, S., Jakobs, G., McDougall, K., Millar, C. I., Naylor, B. J., Parks, C. G., Rew, L. J., & Seipel, T. (2009). Ain't no mountain high enough: plant invasions reaching new elevations. *Frontiers in Ecology and the Environment*, *7*(9), 479-486. <https://doi.org/10.1890/080072>

Pepin, N. C., Arnone, E., Gobiet, A., Haslinger, K., Kotlarski, S., Notarnicola, C., Palazzi, E., Seibert, P., Serafin, S., Schöner, W., Terzago, S., Thornton, J. M., Vuille, M., & Adler, C. (2022). Climate changes and their elevational patterns in the mountains of the world. *Reviews of Geophysics*, *60*(1), e2020RG000730. <https://doi.org/10.1029/2020RG000730>



Pounds, J. A., Fogden, M. P., & Campbell, J. H. (1999). Biological response to climate change on a tropical mountain. *Nature*, 398(6728), 611-615.

<https://doi.org/10.1038/19297>

Schulz, H. M., Thies, B., Chang, S. C., & Bendix, J. (2016). Detection of ground fog in mountainous areas from MODIS (Collection 051) daytime data using a statistical approach. *Atmospheric Measurement Techniques*, 9(3), 1135-1152.

<https://doi.org/10.5194/amt-9-1135-2016>

Schulz, H. M., Li, C. F., Thies, B., Chang, S. C., & Bendix, J. (2017). Mapping the montane cloud forest of Taiwan using 12 year MODIS-derived ground fog frequency data. *PLoS One*, 12(2), e0172663.

<https://doi.org/10.1371/journal.pone.0172663>

Skamarock, W. C., Klemp, J. B., Dudhia, J., Gill, D. O., Barker, D., Duda, M. G., Huang, X., Wang, W., & Powers, J. G. (2008). *A Description of the Advanced Research WRF Version 3* (No. NCAR/TN-475+STR). University Corporation for Atmospheric Research. <http://dx.doi.org/10.5065/D68S4MVH>

Stadtmüller, T. (1987). Cloud forests in the humid tropics: a bibliographic review.

Still, C. J., Foster, P. N., & Schneider, S. H. (1999). Simulating the effects of climate change on tropical montane cloud forests. *Nature*, 398(6728), 608-610.

<https://doi.org/10.1038/19293>

Williams, A. P., Schwartz, R. E., Iacobellis, S., Seager, R., Cook, B. I., Still, C. J., Husak,

G., & Michaelsen, J. (2015). Urbanization causes increased cloud base height and decreased fog in coastal Southern California. *Geophysical Research Letters*, 42(5), 1527-1536. <https://doi.org/10.1002/2015GL063266>.

Yang, X. (2005a). Analysis blending using a spatial filter in grid-point model coupling.

Hirlam Newsletter, 48, 49-55.

Yang, X. (2005b). Background blending using an incremental spatial filter. *Hirlam*

Newsletter, 49, 3-11.

APPENDIX

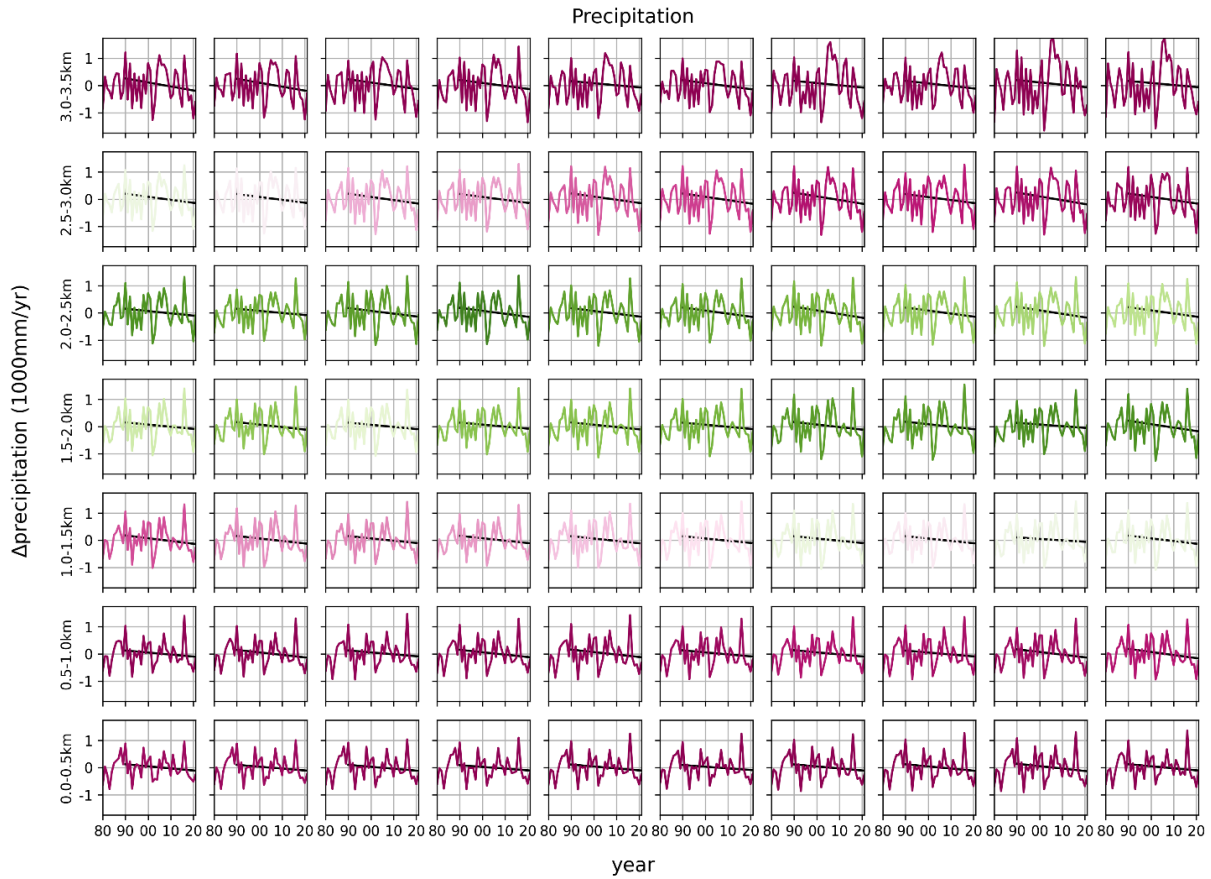


Figure A 1 The time series of annual precipitation (mm/yr) in each group. The panels progress from the lowest elevation in the bottom left to the highest elevation in the top right. Values are the anomalies compared to local climatology. Black lines are the linear fitting for the trend in 1990-2021 in each group. Colors represent the cloud forest fraction averaged for each group, and the scale is the same as in Fig. 2.2c.

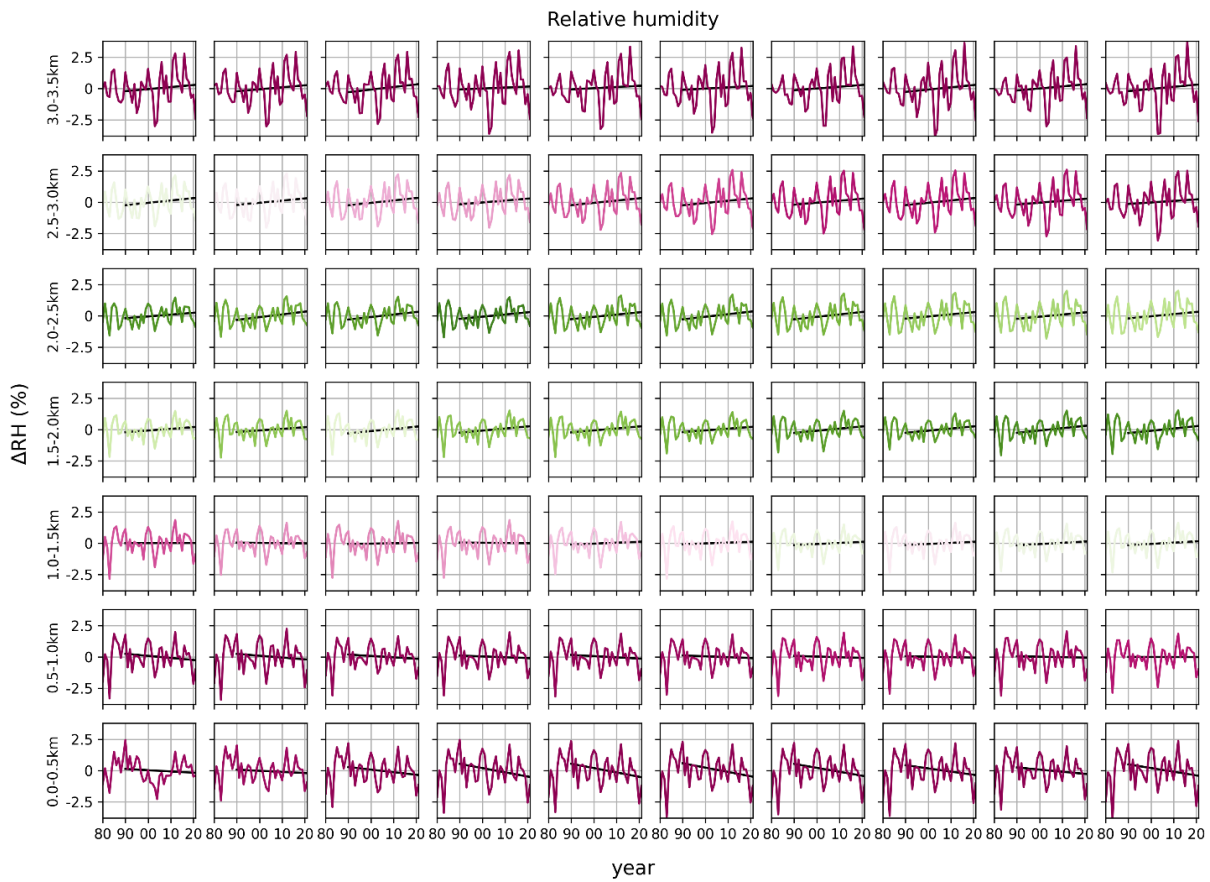


Figure A 2 The time series of relative humidity [RH (%), as a unit] in each group. The panels progress from the lowest elevation in the bottom left to the highest elevation in the top right. Values are the anomalies compared to local climatology. Black lines are the linear fitting for the trend in 1990-2021 in each group. Colors represent the cloud forest fraction averaged for each group, and the scale is the same as in Fig. 2.2c.